

Localization accuracy of compact binary coalescences detected by the third-generation gravitational-wave detectors and implication for cosmology

Wen Zhao^{*}

CAS Key Laboratory for Researches in Galaxies and Cosmology, Department of Astronomy, University of Science and Technology of China, Chinese Academy of Sciences, Hefei, Anhui 230026, China and School of Astronomy and Space Science, University of Science and Technology of China, Hefei 230026, China

Linqing Wen[†]

School of Physics, The University of Western Australia, 35 Stirling Hwy, Crawley, Western Australia 6009, Australia



(Received 28 September 2017; published 26 March 2018)

We use the Fisher information matrix to investigate the angular resolution and luminosity distance uncertainty for coalescing binary neutron stars (BNSs) and neutron star-black hole binaries (NSBHs) detected by the third-generation (3G) gravitational-wave (GW) detectors. Our study focuses on an individual 3G detector and a network of up to four 3G detectors at different locations including the United States, Europe, China, and Australia for the proposed Einstein Telescope (ET) and Cosmic Explorer (CE) detectors. In particular, we examine the effect of the Earth's rotation, as GW signals from BNS and low-mass NSBH systems could be hours long for 3G detectors. In this case, an individual detector can be effectively treated as a detector network with long baselines formed by the trajectory of the detector as it rotates with the Earth. Therefore, a single detector or two-detector networks could also be used to localize the GW sources effectively. We find that a time-dependent antenna beam-pattern function can help better localize BNS and NSBH sources, especially edge-on ones. The medium angular resolution for one ET-D detector is around 150 deg^2 for BNSs at a redshift of $z = 0.1$, which improves rapidly with a decreasing low-frequency cutoff f_{low} in sensitivity. The medium angular resolution for a network of two CE detectors in the United States and Europe, respectively, is around 20 deg^2 at $z = 0.2$ for the simulated BNS and NSBH samples. While for a network of two ET-D detectors, the similar angular resolution can be achieved at a much higher redshift of $z = 0.5$. The angular resolution of a network of three detectors is mainly determined by the baselines between detectors regardless of the CE or ET detector type. The medium angular resolution of BNS for a network of three detectors of the ET-D or CE type in the United States, Europe, and Australia is around 10 deg^2 at $z = 2$. We discuss the implications of our results for multimessenger astronomy and, in particular, for using GW sources as independent tools to constrain the Hubble constant H_0 , the deceleration parameter q_0 , and the equation-of-state (EoS) of dark energy. We find that, in general, if 10 BNSs or NSBHs at $z = 0.1$ with known redshifts are detected by 3G networks consisting of two ET-like detectors, H_0 can be measured with an accuracy of 0.9%. If 1000 face-on BNSs at $z < 2$ are detected with known redshifts, we are able to achieve $\Delta q_0 = 0.002$ for the deceleration parameter, or $\Delta w_a = 0.03$ and $\Delta w_a = 0.2$ for EoS of dark energy, respectively.

DOI: 10.1103/PhysRevD.97.064031

I. INTRODUCTION

The first detection of the gravitational-wave (GW) event GW150914 [1–3], as well as the events GW151226 [4], GW170104 [5], GW170608 [6], GW170814 [7], GW170817 [8], and the less significant candidate LVT151012 [9], marks the beginning of the era of GW

astronomy. Since GWs are expected to be produced in extreme conditions, including the strong gravitational fields, high density regions, and/or extremely early stage of the Universe, and propagate nearly freely in the spacetime once generated, they encode the clean information of these extreme conditions. Currently, the second-generation (2G) ground-based laser interferometer GW detectors are either ongoing and successfully making discoveries of GWs or are expected to be operational in the next few years. This includes Advanced LIGO [10],

*wzhao7@ustc.edu.cn

[†]linqing.wen@uwa.edu.au

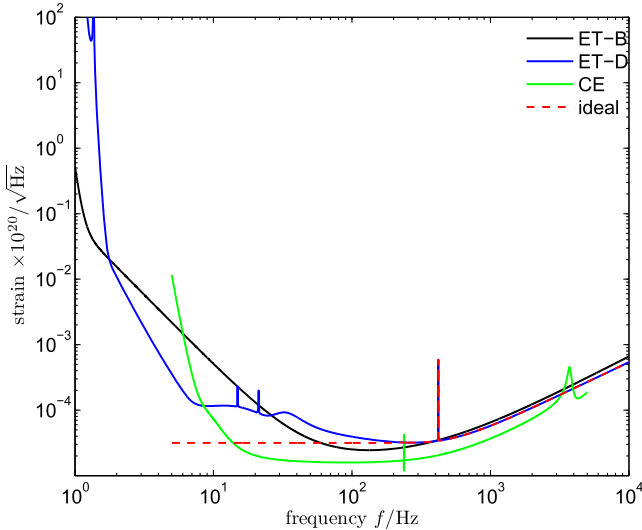


FIG. 1. The amplitude spectral density of ET with ET-B noise level (solid black line) [16], ET with ET-D noise level (solid blue line) [16], CE (solid green line) [17], and the ideal experiment (dashed red line).

Advanced Virgo [11], KAGRA in Japan [12], and the proposed LIGO-India [13].

Looking forward, two leading proposals are currently under consideration for the design of the third-generation (3G) GW detectors (see Fig. 1 for their sensitivity designs). One is the Einstein Telescope (ET), which is a proposed European GW observatory [14–16]. The other is the Cosmic Explorer (CE) [17,18], which is a proposed U.S.-based future GW detector. ET consists of three Michelson interferometers with 10-km-long arms, and interarm angle of 60° , arranged to form an equilateral triangle. Two sensitivity estimates have been put forward for the ET. One is based on a single interferometer covering the full frequency range from 1 Hz to 10 kHz and is referred to as ET-B (Fig. 1, black solid line) [19]. The other one uses the so-called xylophone design [20], in which one GW detector is composed of one cryogenic low-frequency interferometer and one room-temperature high-frequency interferometer. This sensitivity model is referred to as ET-D (Fig. 1, blue solid line). Relative to ET-B, the noise in the sub-10 Hz band of ET-D is substantially reduced. The scientific potentials of ET have been studied by many authors [21–35]. Different from the ET designs, CE (Fig. 1, green solid line) will keep L-shaped configuration, but the length of the arms will be significantly increased to 40 km [17]. In this design, the lower limit of the sensitive band is determined by the seismic and Newtonian noise, the latter of which is still poorly understood [17]. Compared to ET-D, the target sensitivity of CE is significantly better at high frequencies above ~ 8 Hz but ET-D prevails at lower frequencies at around 1–8 Hz. With CE, the horizon redshift of detectable binary black holes (BBHs) will extend to $z \sim 7$, and that of binary neutron stars (BNSs) will be about 2 [18].

The prime candidate sources for both 2G and 3G detectors are GWs produced by coalescing binary systems of compact objects: BNSs, neutron star-black hole (NSBH) binaries, and the BBHs [36]. With more binary coalescence sources expected to be detected with high SNR and at greater distances, it is of paramount interest to use these sources as an independent tool to study the evolution history of the Universe [21,22,37–43], and to test gravity in the strong gravitational fields [3,7,33,44–54]. Accurate localization of these GW sources is crucial to help follow-up observations of their electromagnetic (EM) or neutrino counterparts [2,55] and to increase the chances of identifying their host galaxies and to determine their redshifts. On the other hand, the angular and distance resolutions of an individual 2G detector are rather poor [56]. GW detector network with large baselines is therefore needed to facilitate better source localization [32,57]. However, the tens of square degree nominal angular resolution of 2G detectors still pose a challenge for effective follow-up observations by conventional EM telescopes [58–69]. A network of multiple detectors is also necessary to help measure both GW polarizations, which in turn helps improve the estimation of the source luminosity distance. In addition, a detector network can also help measure the extra polarization modes of GW allowed in more general theories of gravitation, which is of crucial importance to test gravity in strong gravitational fields [70–72].

One key difference between the proposed 3G and 2G detectors is that the proposed 3G detectors are expected to have extended sensitivity at lower frequencies than 2G detectors. For ET-D, the cutoff of the low-frequency sensitivity is extended to $f_{\text{low}} \sim 1$ Hz. The time to coalescence of a BNS is a function of $f_{\text{low}}^{-8/3}$. The BNS signals can therefore be in band for 3G detectors for several hours, or even for several days compared to tens of minutes in the 2G detector band. Thus, the time dependence of the detector beam-pattern functions of the 3G detectors, due to the motion of the Earth, could become important. With this effect, an individual detector can be effectively treated as a network including a set of detectors at different locations along the detector's trajectory on the Earth, which observe a given GW event at different time. The baseline of this ‘network’ is determined by the duration of the event in the detector's band. If the duration can be around one day, the baseline is roughly the Earth's diameter. We therefore anticipate a significant improvement in parameter estimation, especially that related to the localization for detectors with significant low-frequency sensitivity.¹

¹We should emphasize that, in addition to the loss of the localization, the bias of the parameter estimation might also be induced, if ignoring the time dependence of the detector antenna beam-pattern functions. However, in order to address this issue, the Monte Carlo analyzes instead of the Fisher matrix analyzes are needed, which is beyond the scope of the present work.

Several algorithms, including numerical computations and analytical expressions, have been developed to quantify the effectiveness of GW detector networks [58–68]. In this article, we use the standard Fisher matrix technique to investigate the angular resolution and luminosity distance determination of a single 3G detector as well as a network of multiple detectors including ET, CE, ET-like and/or CE-like detectors at different locations.² We also demonstrate the potential capabilities of utilizing the accurate localization of GW sources to constrain the cosmological parameters, including the Hubble constant, the deceleration parameter and the equation-of-state (EoS) of cosmic dark energy. In addition, to study the effect of low-frequency sensitivity, we also include an ideal detector (Fig. 1, red dashed line) with a better low frequency sensitivity than ET-D. The detector is designed to have a constant sensitivity across the frequency band of $f \in [5, 400]$ Hz with the noise power spectral density $S_I(f) = 10^{-49}$ /Hz and infinity at $f < 5$ Hz.

This paper is organized as follows. In Sec. II, we review the mathematical preliminaries of GW waveforms from binary coalescence and the response of GW detectors to these signals. In Sec. III, we describe our method to calculate the Fisher matrix for a set of nine parameters required to fully describe a GW signal from compact binary coalescence. A comparison with a previously published result is presented to verify the validity of our calculation. In Sec. IV we show the result for one 3G detector from numerical simulations for both BNS and NSBH sources. We demonstrate the dependence of the angular resolution and distance determination on the low-frequency cutoff of the detector. In Sec. V, we present the localization of GW sources at different redshifts observed by an individual 3G detector, and by a network of two to four 3G detectors. In Sec. VI, we discuss the implications for cosmology in the 3G detector era. At the end, in Sec. VII, we summarize our main results.

Throughout this paper, we choose the units in which $G = c = 1$, where G is the Newtonian gravitational constant, and c is the speed of light in vacuum.

II. GW WAVEFORMS AND THE DETECTOR RESPONSE

As a general consideration, we assume that a GW event is observed by a ground-based network, which includes N_d GW detectors, each with spatial size much smaller than the GW wavelength.³ The spatial locations of the detectors are given by the vector \mathbf{r}_I with $I = 1, 2, \dots, N_d$. In the celestial coordinate system, the vector \mathbf{r}_I is given by

²In finishing this paper, we find a parallel independent work [73] that has some overlap with our calculation of the angular resolution for a network of more than two 3G detectors.

³In the recent paper [74], the authors discussed the effects when the GW frequencies are comparable to the round-trip light travel time down the detector arms.

TABLE I. The coordinates of the interferometers used in this study. Orientation is the smallest angle made by any of the arms and the local north direction [32].

	φ	λ	γ	ζ
Einstein Telescope in Europe	43.54°	10.42°	19.48°	60°
Cosmic Explorer in the U.S.	30.54°	-90.53°	162.15°	90°
Assumed detector in Australia	-31.51°	115.74°	0°	—
Assumed detector in China	38.39°	104.28°	89.95°	—

$$\mathbf{r}_I = R_{\oplus}(\sin \varphi_I \cos \alpha_I, \sin \varphi_I \sin \alpha_I, \cos \varphi_I), \quad (1)$$

where R_{\oplus} is the radius of the Earth, φ_I is the latitude of the detector. The angle α_I is defined as $\alpha_I \equiv \lambda_I + \Omega_r t$, where λ_I is the east longitude of the detector, Ω_r is the rotational angular velocity of the Earth. Note that, throughout this paper, we fix $t = 0$ at which the Greenwich sidereal time is zero.

For an individual detector labeled by I , the response to an incoming GW signal is a linear combination of two wave polarizations in the transverse-traceless gauge,

$$d_I(t_0 + \tau_I + t) = F_I^+ h_+(t) + F_I^\times h_\times(t), \quad 0 < t < T, \quad (2)$$

where h_+ and h_\times are the plus and cross modes of GW, respectively, t_0 is the arrival time of the wave at the coordinate origin and τ_I is the time required for the wave to travel from the origin to reach the I th detector at time t ,

$$\tau_I(t) = \mathbf{n} \cdot \mathbf{r}_I(t). \quad (3)$$

Here \mathbf{n} is the propagation direction of a GW, $t \in [0, T]$ is the time label of the wave, and T is the signal duration. The quantities F_I^+ and F_I^\times are the detector's antenna beam-pattern functions, which depend on the source location (θ_s, ϕ_s) , the polarization angle ψ_s , the detector's location on the Earth labeled by latitude φ , longitude λ , the angle γ , which determines the orientation of the detector's arms with respect to local geographical directions: γ is measured counter-clockwise from East to the bisector of the interferometer arms, as well as the angle between the interferometer arms ζ . See in Table I [32] for the parameters used for the potential Einstein Telescope (ET) in Europe, Cosmic Explorer (CE) experiment in the U.S., the assumed detector in Australia, and that in China, respectively. For the ground-based detectors, the expressions of F_I^+ and F_I^\times are explicitly given in [75], which are periodic functions of time with a period equal to one sidereal day, due to the diurnal motion of the Earth.

During the inspiral phase of the binary coalescence, the change in orbital frequency over a single GW cycle is negligible; it is, therefore, possible to apply a stationary

phase approximation (SPA) to compute the Fourier transformation. We denote the Fourier transform of the function $B(t)$ as $B(f)$. Given a function $B(t)=2A(t)\cos\phi(t)$, where $d\ln A/dt \ll d\phi(t)/dt$ and $|d^2\phi/dt^2| \ll (d\phi/dt)^2$, the SPA provides the following estimate of the Fourier transformation $B(f)$ [33,76]:

$$B(f) \simeq \frac{A(t_f)}{\sqrt{F(t_f)}} e^{i[\Psi_f(t_f)-\pi/4]}, \quad f \geq 0, \quad (4)$$

where $\Psi_f(t) \equiv 2\pi ft - \phi(t)$, $2\pi F(t) \equiv d\phi/dt$. In this formula, t_f is defined as the time at which $F(t_f) = f$ and $\Psi_f(t_f)$ is the value of $\Psi_f(t)$ at $t = t_f$. Employing SPA, the Fourier transform of the time-series data from the I th GW detector can be obtained as follows:

$$d_I(f) = \int_0^T d_I(t) e^{2\pi i f t} dt. \quad (5)$$

Denoting the corresponding one-side noise spectral density by $S_I(f)$, we define a whitened data set in the frequency domain [65]:

$$\hat{d}_I(f) \equiv S_I^{-1/2}(f) d_I(f). \quad (6)$$

For a detector network, this can be rewritten as [65]

$$\hat{\mathbf{d}}(f) = e^{-i\Phi} \hat{\mathbf{A}} \mathbf{h}(f), \quad (7)$$

where Φ is the $N_d \times N_d$ diagonal matrix with $\Phi_{IJ} = 2\pi f \delta_{IJ}(\mathbf{n} \cdot \mathbf{r}_I(f))$, and

$$\begin{aligned} \hat{\mathbf{A}} \mathbf{h}(f) &= \left[\frac{F_1^+ h_+(f) + F_1^\times h_\times(f)}{\sqrt{S_1(f)}}, \frac{F_2^+ h_+(f) + F_2^\times h_\times(f)}{\sqrt{S_2(f)}}, \right. \\ &\quad \ldots, \left. \frac{F_{N_d}^+ h_+(f) + F_{N_d}^\times h_\times(f)}{\sqrt{S_{N_d}(f)}} \right]^T. \end{aligned} \quad (8)$$

Note that, F_I^+ , F_I^\times , Φ_{ij} are all functions with respect to frequency, in general, due to the diurnal motion of the Earth. With SPA, these functions are simply given by

$$\begin{aligned} F_I^+(f) &= F_I^+(t = t_f), & F_I^\times(f) &= F_I^\times(t = t_f), \\ \Phi_{ij}(f) &= \Phi_{ij}(t = t_f), \end{aligned} \quad (9)$$

where $t_f = t_c - (5/256)\mathcal{M}_c^{-5/3}(\pi f)^{-8/3}$ [76],⁴ \mathcal{M}_c is the chirp mass of binary system, which will be defined in next paragraph, and t_c is the binary coalescence time. If the effect of the Earth's rotation is ignored, these can be approximately treated as constants for a given GW event.

⁴Note that this relationship is untenable in the general modified gravities [33].

In this paper, we consider both cases to show the effect of the Earth's rotation.

In general, the spinning inspiral-merge-ringdown coalescence waveform template of the compact binaries is needed for the parameter estimation. In order to simplify and speed up the calculation, similar to previous works [21,22,33], in this paper we adopt the restricted post-Newtonian (PN) approximation of the waveform for the nonspinning systems [36,77,78], which includes only waveforms in the inspiralling stage. Compared with the case with full waveforms, we do not expect a significant change in our result. For a coalescing binary at a luminosity distance d_L , with component masses m_1 and m_2 , total mass $M = m_1 + m_2$, symmetric mass ratio $\eta = m_1 m_2 / M^2$ and "chirp mass" $\mathcal{M}_c = M \eta^{3/5}$, the SPA Fourier transform of a GW waveform is given by [36]

$$\begin{aligned} &F_I^+ h_+(f) + F_I^\times h_\times(f) \\ &= \mathcal{A}_I f^{-7/6} \exp[i(2\pi f t_c - \pi/4 + 2\psi(f/2)) - \varphi_{I,(2,0)}], \end{aligned} \quad (10)$$

with the Fourier amplitude \mathcal{A}_I given by

$$\begin{aligned} \mathcal{A}_I &= \frac{1}{d_L} \sqrt{((F_I^+(1 + \cos^2 \iota))^2 + (2F_I^\times \cos \iota)^2} \\ &\quad \times \sqrt{5\pi/96} \pi^{-7/6} \mathcal{M}_c^{5/6}, \end{aligned} \quad (11)$$

where ι is the inclination angle between the binary's orbital angular momentum and the line of sight. We use the 3.5 PN approximation for the phase [36,78], where the functions ψ and $\varphi_{I,(2,0)}$ are given by

$$\psi(f) = -\psi_c + \frac{3}{256\eta} \sum_{i=0}^7 \psi_i (2\pi M f)^{i/3}, \quad (12)$$

$$\varphi_{I,(2,0)} = \tan^{-1} \left(-\frac{2 \cos \iota F_I^\times}{(1 + \cos^2 \iota) F_I^+} \right). \quad (13)$$

The parameters ψ_i can be found in [36]. The upper cutoff frequency f_{up} is calculated from the last stable orbit, which marks the end of the inspiral regime and the onset of the final merge. We will assume that this occurs when the radiation frequency reaches $f_{\text{up}} = 2f_{\text{LSO}}$, with $f_{\text{LSO}} = 1/(6^{3/2} 2\pi M)$ the orbital frequency at the last stable orbit. Note that, for GW sources at redshift z , the observed mass m is related to the physical (intrinsic) mass m_{phys} by the relation $m = (1+z)m_{\text{phys}}$. Throughout this paper, all the masses refer to the observed quantity unless explicitly specified.

III. FISHER INFORMATION MATRIX AND ANALYSIS METHOD

By maximizing the correlation between a template waveform that depends on a set of parameters and a measured signal, the matched filtering provides a natural way to estimate the parameters of the signal and their errors. With a given detector noise $S_I(f)$, we employ the Fisher matrix approach in this paper. In the case of a network including N_d independent GW detectors, the Fisher matrix is given by [79]

$$\Gamma_{ij} = \langle \partial_i \hat{\mathbf{d}} | \partial_j \hat{\mathbf{d}} \rangle, \quad (14)$$

where $\partial_i \hat{\mathbf{d}} \equiv \partial \hat{\mathbf{d}}(f) / \partial p_i$, and p_i denote the free parameters to be estimated. For any given binary system, the response of GW detector in Eq. (7) depends on nine system parameters ($\mathcal{M}_c, \eta, t_c, \psi_c, i, \theta_s, \phi_s, \psi_s, d_L$), where ψ_c is defined in Eq. (12), and the other parameters are all defined previously. The angular brackets denote the scalar product, which, for any two functions $a(t)$ and $b(t)$ is defined as

$$\langle a, b \rangle = 2 \int_{f_{\text{low}}}^{f_{\text{up}}} \{ \tilde{a}(f) \tilde{b}^*(f) + \tilde{a}^*(f) \tilde{b}(f) \} df. \quad (15)$$

Under the assumption of stationary Gaussian detector noise, the optimal squared signal-to-noise ratio (SNR) is given by

$$\rho^2 = \langle \hat{\mathbf{d}} | \hat{\mathbf{d}} \rangle. \quad (16)$$

The Fisher matrix is commonly used in many fields [80] to estimate errors in the measured parameters by the expression $\langle \delta p_j \delta p_k \rangle = (\Gamma^{-1})_{jk}$. Once the total Fisher matrix Γ_{ij} is calculated, an estimate of the root mean square (RMS) error, Δp_i , in measuring the parameter p_i can then be calculated,

$$\Delta p_i = (\Gamma^{-1})_{ii}^{1/2}. \quad (17)$$

The correlation coefficient for any two parameters p_i and p_j is quantified by the ratio $r_{ij} \equiv (\Gamma^{-1})_{ij}/((\Gamma^{-1})_{ii}(\Gamma^{-1})_{jj})^{1/2}$, and the result of $r_{ij} = 0$ indicates the no correlation between them. Note that, if any two parameters are completely correlated, i.e. they are degenerate in data analysis, the Fisher matrix is not invertible. The use of the Fisher matrix to estimate parameter uncertainties is based on the following theorem. The Cramer-Rao bound states that for an unbiased estimator (the ensemble average of which is the true value), the Fisher matrix sets a method-independent lower bound for the covariance matrix of estimated parameters when considering statistical errors [81].

In the calculation of the Fisher matrix, the quantity $\partial \hat{\mathbf{d}}(f) / \partial p_i$ usually has no analytical expression, and need to be numerically calculated. We adopt the approximation $\partial \hat{\mathbf{d}}(f) / \partial p_i \simeq (\hat{\mathbf{d}}(f; p_i + \delta p_i) - \hat{\mathbf{d}}(f; p_i)) / \delta p_i$ and numerically calculate the elements of the Fisher matrix for each

GW event. To guarantee the reliability of our calculation, for each GW detector, we vary the values of δp_i until this approximation becomes stable, i.e. increasing or decreasing each value of δp_i by a factor of 10, the Fisher matrix has no significant change. Note that the Fisher matrix yields only the lower limit of the covariance matrix. In reality, a parameter estimation method would have encountered issues such as the well-known multimodality problem [2,8] and may or may not reach the limit prescribed by the Fisher matrix.

For each GW event observed by the network, we calculate the nine-parameter Fisher matrix and marginalize it to the one with two position parameters (θ_s, ϕ_s) , which are the colatitude and longitude in a polar coordinate system, respectively. The covariance matrix is given by the inverse of Fisher matrix, and the error in solid angle (measured in steradians) is given by

$$\Delta\Omega_s = 2\pi |\sin \theta_s| \sqrt{\langle \Delta\theta_s^2 \rangle \langle \Delta\phi_s^2 \rangle - \langle \Delta\theta_s \Delta\phi_s \rangle^2}, \quad (18)$$

where $\Delta\theta_s$ and $\Delta\phi_s$ are the deviations of θ_s and ϕ_s from their true values, and the quantities $\langle \Delta\theta_s^2 \rangle$, $\langle \Delta\phi_s^2 \rangle$ and $\langle \Delta\theta_s \Delta\phi_s \rangle$ are given in the nine-parameter covariance matrix. The uncertainty of $\ln d_L$ is straightly derived by employing the formula in Eq. (17).

Throughout this paper, we simulate numerically binary coalescence signals with random binary orientations and sky directions for our investigations. We also generate the random samples at every redshift with a 0.1 spacing within a specified range, and the luminosity distance is calculated with a standard Λ CDM cosmology [82] assumed. The sky direction, binary inclination and polarization angle of these binaries are randomly chosen in the angular ranges of $\cos\theta_s \in [-1, 1]$, $\phi_s \in [0, 360^\circ]$, $\psi_s \in [0, 360^\circ]$ and $\cos i \in [-1, 1]$. Without loss of generality, the merger time of these samples are chosen to be $t_c = 0$. The detection criteria is chosen to have the optimal network SNR ≥ 8 .

To demonstrate the effectiveness of our Fisher matrix technique, we compare our method to the Markov chain Monte Carlo (MCMC) analysis used in [32], which analyzed the localization of GW sources with the nested sampling flavor of lalinference [67] for 3G detectors with $f \geq 10$ Hz. Similar to [32], we simulate 50,000 random BBH samples, and assume that the total physical mass of each BBH is uniformly distributed in the range of $[12, 40] M_\odot$ with a minimum mass ratio of $1/3$.⁵ The redshifts are uniformly distributed in comoving volume, assuming a standard Λ CDM cosmology [82], in the range

⁵For the BBHs with larger masses $M_{\text{phys}} \gtrsim 40 M_\odot$, the high-frequency cutoff f_{LSO} of the restricted PN approximation of the waveform is smaller than 50 Hz and the ring-down signals become important, so the PN approximation becomes unsuitable for 3G detectors. We, therefore, do not consider these events.

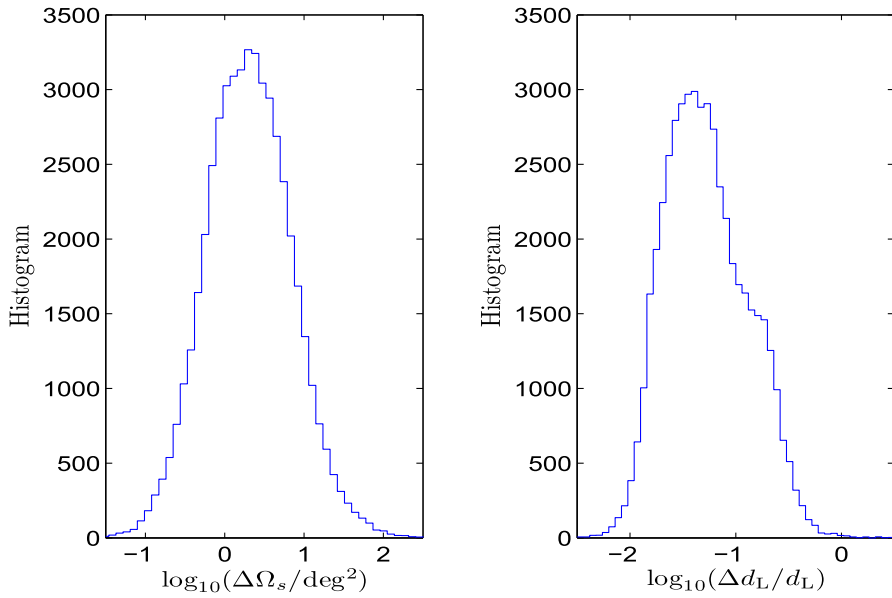


FIG. 2. The histograms of $\Delta\Omega_s$ (left panel) and $\Delta d_L/d_L$ (right panel) for 50,000 BBH samples, which are distributed in the redshift range $z \in [0, 3]$ (see the main text for the details).

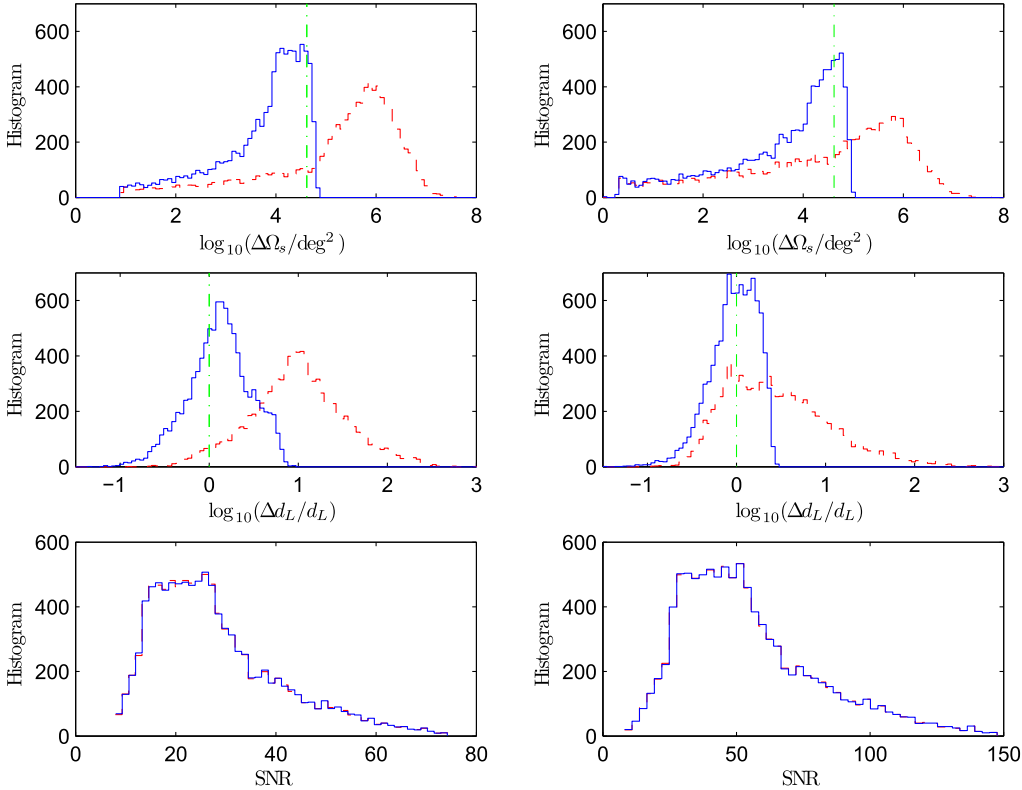


FIG. 3. Distribution of the ET-B angular resolution $\Delta\Omega_s$ (upper), distance determination accuracy $\Delta d_L/d_L$ (middle) and optimal SNR (lower) with (blue solid lines) and without (red dashed lines) considering the Earth's rotation for the $(1.4 + 1.4) M_\odot$ BNS systems (left panels) and for the $(1.4 + 10) M_\odot$ NSBH systems (right panels) at a distance of 1 Gpc.

$z \in [0, 3]$. We calculate the two-detector network SNR values of these binaries for a network of an ET-D in Europe and a CE in the U.S. (Fig. 1), and select the sources with SNRs in the range of $[10, 600]$ as in [32]. Our

results are shown in Fig. 2 for the distribution of the angular resolution $\Delta\Omega_s$ and distance uncertainty $\Delta d_L/d_L$. These results are comparable to that in Fig. 3 and Fig. 4 in [32] from the MCMC analysis. While the Fisher matrix

yields a lower limit for the covariance matrix for parameter estimation, which cannot always be achieved, it represents a simple, method-independent, and reasonable estimate for the detection and localization capability for future experiments and is especially helpful for comparing results of parameter estimation among different experiments.

IV. EFFECT OF LOW-FREQUENCY SENSITIVITY

Consideration of the angular resolution of a 3G detector is different from a 2G detector in two possible aspects besides the increased SNRs due to better sensitivity. (1) An ET-like detector contains three colocated independent V-shaped Michelson interferometers with an opening angle of 60° and rotated relative to each other by 120° . The three V-shaped interferometers are equivalent, in terms of antenna beam-pattern and sensitivity, to two colocated L-shaped interferometers whose arms are three-quarters in length and rotated relative to each other by an angle of 45° . It has essentially no blind spots in the sky [26]. Therefore, the directional sensitivity is greatly improved [83] over the L-shaped 2G detector. In addition, GW polarizations and polarization angle [83] can be determined by one 3G detector. (2) Extended lower frequency sensitivity is expected for the 3G detectors [84]. Therefore, the observed GW signal duration is possibly a significant fraction of the Earth's rotation period. The angular resolution of the detector can therefore be improved by the non-negligible GW energy-flux weighted geometrical area formed by the trajectory of the detector due to the Earth self rotation within the signal duration. This is similar to the case for the angular resolution for the space-based detector LISA as discussed in Wen and Chen (2010) [65], (see also in [85,86]).

For binary coalescence, the duration of the signal t_* in a detector band is a strong function of the detector's low-frequency cutoff f_{low} [76],

$$t_* = 0.86 \text{ day} \left(\frac{1.21 M_\odot}{M_c} \right)^{5/3} \left(\frac{2 \text{ Hz}}{f_{\text{low}}} \right)^{8/3}, \quad (19)$$

where M_c is the chirp mass of the system. For the BNS with $m_1 = m_2 = 1.4 M_\odot$, we have $t_* = 0.28$ hours for $f_{\text{low}} = 10 \text{ Hz}$, $t_* = 0.29$ days for $f_{\text{low}} = 3 \text{ Hz}$, and $t_* = 5.44$ days for $f_{\text{low}} = 1 \text{ Hz}$. This evaluation shows that if the sensitivity for GWs at $f \lesssim 10 \text{ Hz}$ is non-negligible, the Earth's rotation will play a crucial role for the localization of GW sources. For sources with higher masses (e.g., BBH, NSBH), the effect of Earth's rotation becomes important at lower f_{low} than the BNS systems. However, the duration of GW signals in the detector frequency band is too short for the low- f effect to be significant. For instance, for a BBH system with $m_1 = m_2 = 30 M_\odot$, which is similar to that of GW150914, we have $t_* = 0.79$ hours for $f_{\text{low}} = 1 \text{ Hz}$,

therefore the effect of the Earth's rotation is expected to be small. For this reason, in this article, we only consider the compact binary systems of BNSs and NSBHs with small black hole masses.

A. Effect of the Earth's rotation

We first demonstrate the importance of considering the time-dependent antenna beam-pattern function due to the Earth's rotation when calculating the angular resolution and distance uncertainties of BNSs and NSBHs for 3G detectors with the proposed design of ET-B, CE, and ET-D. To illustrate our point, we compare the angular resolution between the following two cases when calculating the Fisher matrix Γ_{ij} . (1) Constant antenna beam-pattern functions and time delay between detectors, that is fixing the F_I^+ , F_I^\times , and Φ values in Eq. (7) at $t = 0$ (Figs. 3–5, red dashed lines), and (2) t -dependent (or f -dependent) F_I^+ , F_I^\times , and Φ in Eq. (7) (Figs. 3–5, blue solid lines). The comparisons are conducted for the detected BNS and NSBH sources from a set of 10^4 randomly sampled (Sec. III) BNS and NSBH sources, respectively, at a luminosity distance of 1 Gpc.

We find that for the BNS systems (Fig. 3, left panels), without considering the time dependence of the antenna beam-pattern functions (Fig. 3, red dashed lines), ET-B alone cannot localize most of the GW sources at this distance, even at high SNRs. However, if taking into account the time dependence (Fig. 3, blue solid lines), while the SNR values are largely unchanged (Fig. 3, bottom panels), around 20% BNS sources can be localized with $\Delta\Omega_s < 10^3 \text{ deg}^2$, and 14% sources have a distance uncertainty $\Delta d_L/d_L < 50\%$. Similar result can be found for the NSBH systems but with less significant effect due to the overall shorter duration of these sources (Fig. 3, right panels).

The effect of considering time-dependent antenna beam-pattern functions for a CE can be found in Fig. 4 for the same sample of sources. The SNR values (lower panels) are significantly larger for CE than those for the ET-B, due to its much better sensitivity around 100 Hz. The effect of the Earth's rotation on CE is still noticeable, but much less pronounced (upper and middle panels) than ET-B, as CE has a poorer sensitivity in the sub-5 Hz low-frequency range than ET-B. Both the angular resolution and distance accuracy of the BNS and NSBH detected by the CE are overall much worse than ET-B despite the much larger SNRs. This is understandable as CE is designed to be very similar to a 2G detector, but with a much improved sensitivity. It therefore has similarly poor single-detector directional sensitivity as a 2G detector. In comparison, ET-B has the advantages of being equivalent to two L-shaped detectors plus better low frequency sensitivity. In other words, the time dependence of the antenna beam-pattern function and the design of ET help better determine

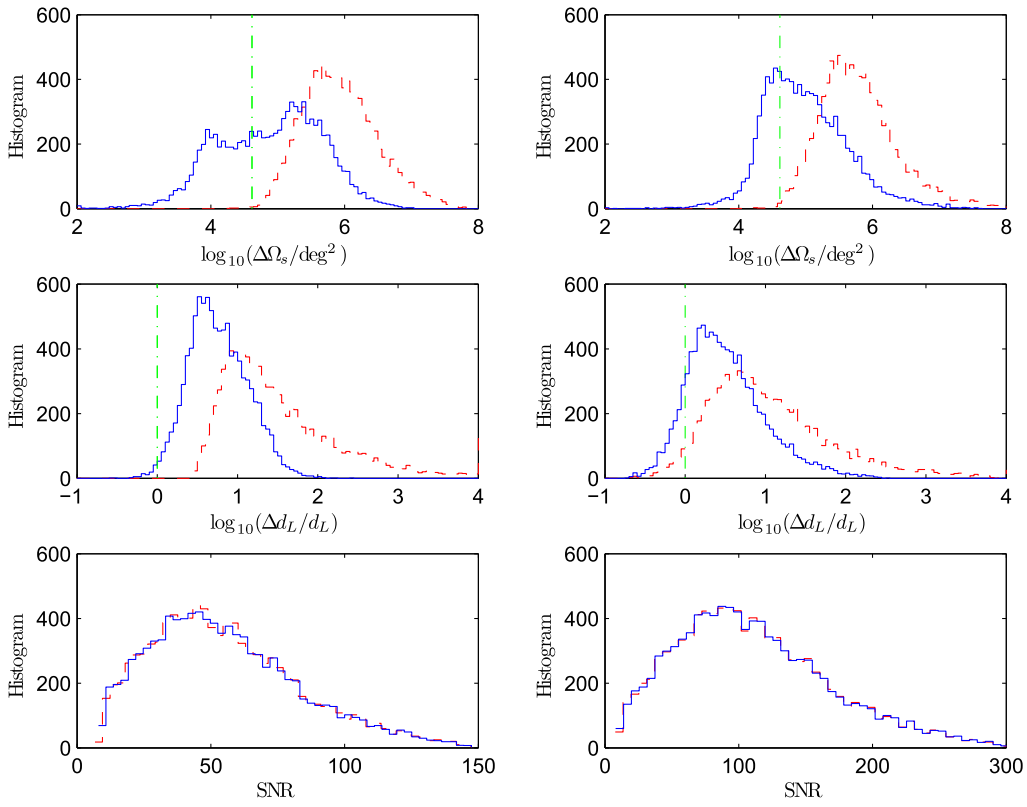


FIG. 4. Same as Fig. 3, but for CE.

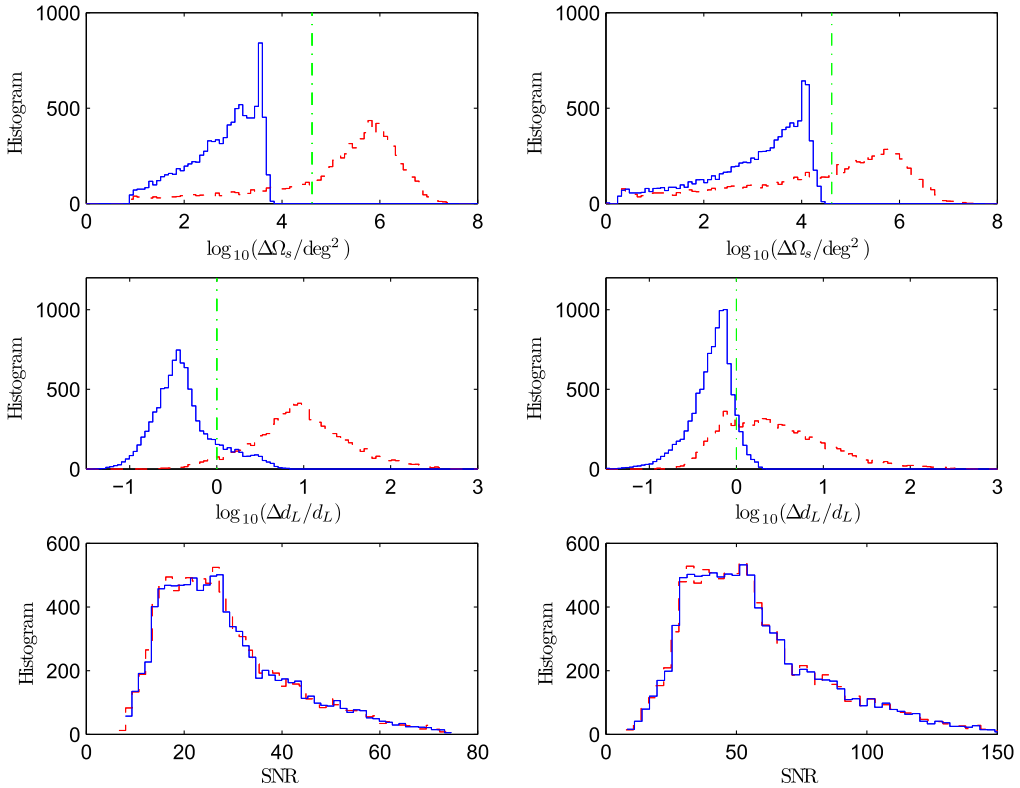


FIG. 5. Same as Fig. 3, but for ET-D.

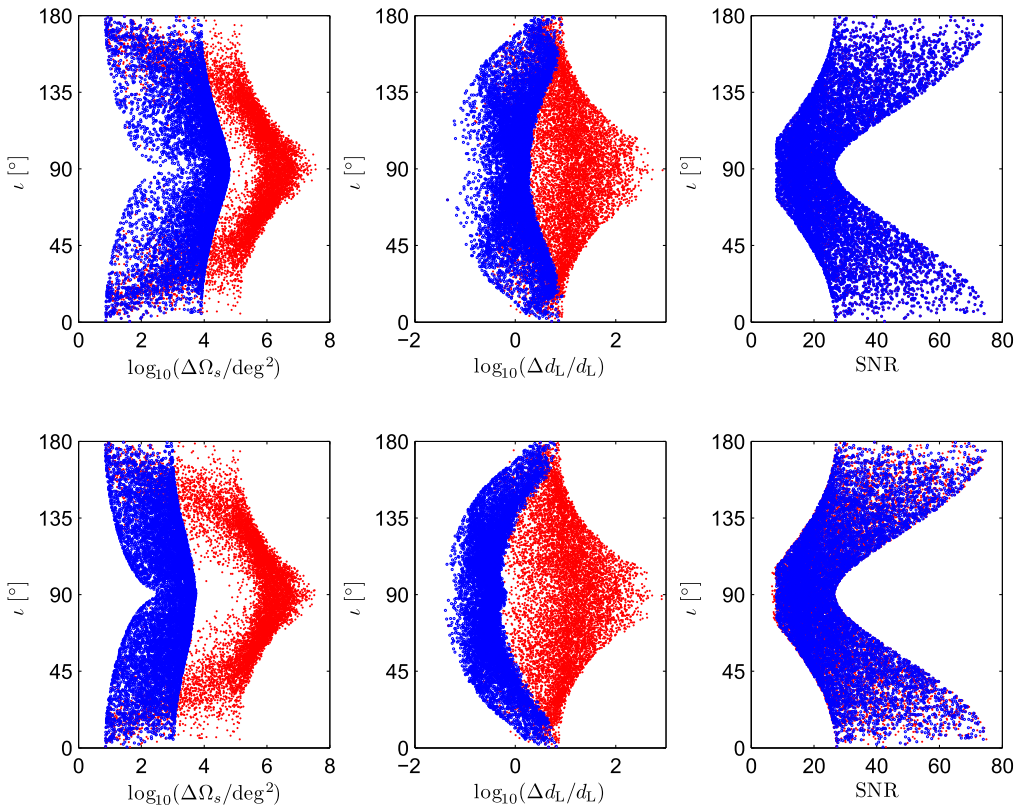


FIG. 6. The distributions of $\Delta\Omega_s$ (left), $\Delta d_L/d_L$ (middle) and SNR (right) with respective to the inclination angle i for 10^4 BNS samples at the distance $d_L = 1$ Gpc. The upper panels show the results of ET detector with ET-B noise, and the lower ones show those of ET detector with ET-D noise. In each panel, the red dots indicate the distribution of samples in the case without considering the Earth's rotation, and the blue circles indicate that in the case with considering the Earth's rotation.

the wave polarizations and merger time which in turn help the source localization.

The influence of the Earth's rotation is much more prominent in ET-D (Fig. 5) than in ET-B, as expected from its much lower noise level at low frequencies of $f \in (2, 20)$ Hz. The angular resolutions of $\Delta\Omega_s$ in ET-D are 1 order of magnitude smaller than in ET-B, and the distance determination accuracy $\Delta d_L/d_L$ is nearly 3 times better. Nearly 50% BNS systems can be localized within 1000 deg^2 at $d_L = 1$ Gpc with one single ET-D. This, when scaled with distance, is comparable to the localization accuracy of their first detected GW source GW150914 by the two Advanced LIGO detectors during the first science run. Around 20% of BNSs can possibly be localized within 100 deg^2 by an ET-D while the distance accuracy is well within 30%. For NSBH systems, the angular resolution and distance determination are slightly worse than the BNS systems.

The effect of the Earth's rotation on the dependence of the angular resolution, the distance uncertainty and SNR with the binary inclination angle i is also shown for the same 10^4 BNS samples at 1 Gpc for an ET-B (Fig. 6, upper panels), an ET-D (Fig. 6, lower panels), a CE detector (Fig. 7, upper panels), and for two CE detectors

in Europe and the U. S., respectively (Fig. 7, lower panels). The angular resolution of face-on ($i \sim 0^\circ$ or 180°) binaries is overall better than those edge-on systems ($i \sim 90^\circ$) due to larger SNR values. This is desirable for EM observations of BNS systems associated with on-axis gamma-ray bursts (GRBs). On the other hand, the time-dependent antenna beam-pattern functions can help better localize those edge-on systems whose GRB counterparts are less likely to be observed at high SNRs as the GRB jet opening angles are expected to be small. Such improvement is much more pronounced in the ETs than in CE due to ET's better low frequency sensitivity.

From Figs. 3–5, we find that there is a significant fraction of samples, where both the sky position and the luminosity distance cannot be resolved, even if we consider the effect of the Earth's rotation. Note that these results are derived from the GW observation alone. If one can identify the EM counterparts of GW events by the coincidence of their arrival times, the sky position θ_s, ϕ_s (and i, ψ for the face-on sources) can be determined in advance, the errors of luminosity distance d_L can then be significantly reduced [22] and the bimodal distribution of parameters in realistic analysis could be solved [8].

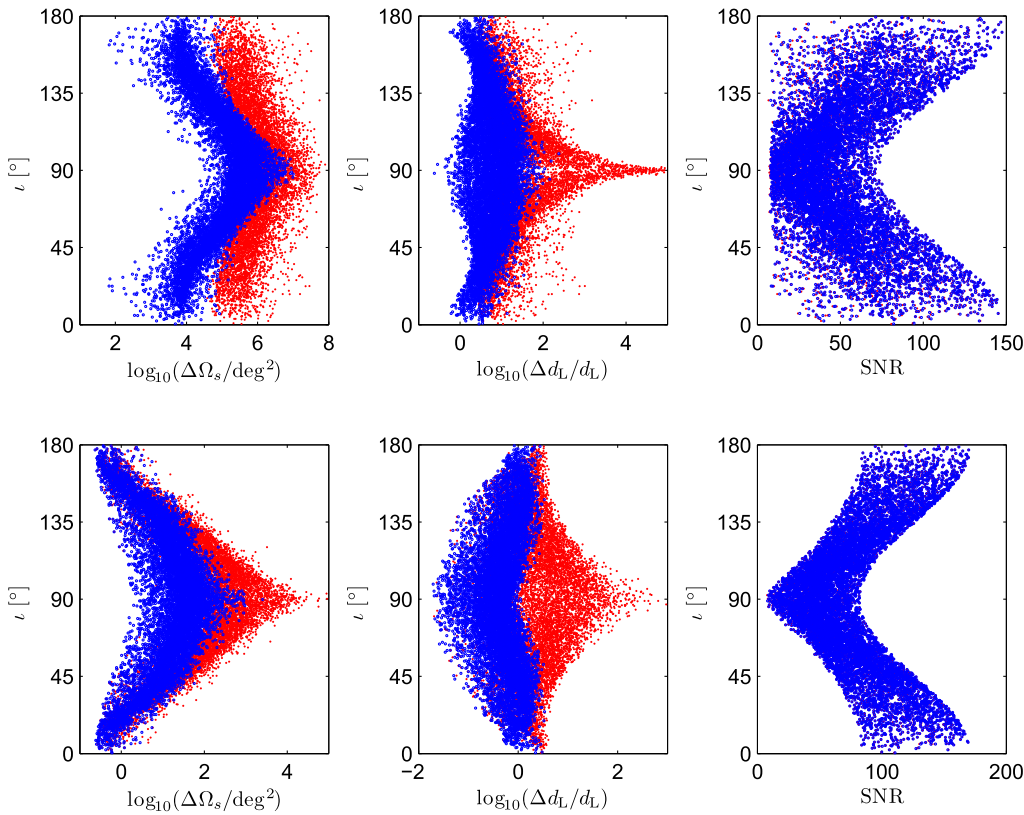


FIG. 7. Same as Fig. 6, but the upper panels show the results of CE, and the lower panels show those of the 2CE detector network.

B. Dependence of angular resolution and distance accuracy on f_{low}

The effect of the Earth's rotation on the angular resolution of a 3G detector is similar to that of the space-based detector LISA [65,85,86]. For LISA, the angular resolution follows roughly a broken power of the observation time with turn-around time near the period of the Earth around the Sun. This is because the angular resolution is inversely proportional to the projected geometrical area weighted by GW flux in the direction normal to the wave direction formed by the trajectory of the detector. Once the signal is much longer than the Earth's rotation period around the Sun, the project area is approximately a constant therefore the angular resolution improves mainly due to accumulated SNRs. For a 3G detector, as the rotation of the Earth is important, we expect to observe similar approximate broken power-law dependence of the angular resolution to the observing duration, or in this case, the low-frequency cutoff. The turn-around frequency is expected to be around the frequency when the signal duration is comparable to the Earth self-rotation period.

As a proof of principle, we first demonstrate the effect of f_{low} on the angular resolution and distance determination using an ideal detector (Fig. 8) similar to that described in Fig. 1 but with flat noise level extended to the entire frequency band. We show the results for BNS (left panels) and NSBH (right panels) at 1 Gpc at two randomly chosen

sky directions (Fig. 8, green circles and blue triangles) with random binary orientations, as well as the median values of a random sample of 10^4 sources over different sky directions and binary orientations (Fig. 8, red asterisks). A pronounced broken power-law relation can be observed for the angular resolution and distance determination independent of the source sky directions. The turn-around frequencies for the broken power-law are around 2 Hz, and 1 Hz for the BNS and NSBH sources, respectively, around which the signal duration is comparable to the Earth's rotation period. Specifically, we found for the BNS systems,

$$\log_{10}(\Delta\Omega_s/\text{deg}^2) = \begin{cases} -0.12 + 1.36(x - x_0), & f \leq 2 \text{ Hz}, \\ -0.12 + 4.96(x - x_0), & f > 2 \text{ Hz}, \end{cases} \quad (20)$$

$$\log_{10}(\Delta d_L/d_L) = \begin{cases} -1.95 + 0.50(x - x_0), & f \leq 2 \text{ Hz}, \\ -1.95 + 2.68(x - x_0), & f > 2 \text{ Hz}, \end{cases} \quad (21)$$

and for NSBH,

$$\log_{10}(\Delta\Omega_s/\text{deg}^2) = \begin{cases} -1.17 + 1.35(x - x_0), & f \leq 1 \text{ Hz}, \\ -1.17 + 4.71(x - x_0), & f > 1 \text{ Hz}, \end{cases} \quad (22)$$

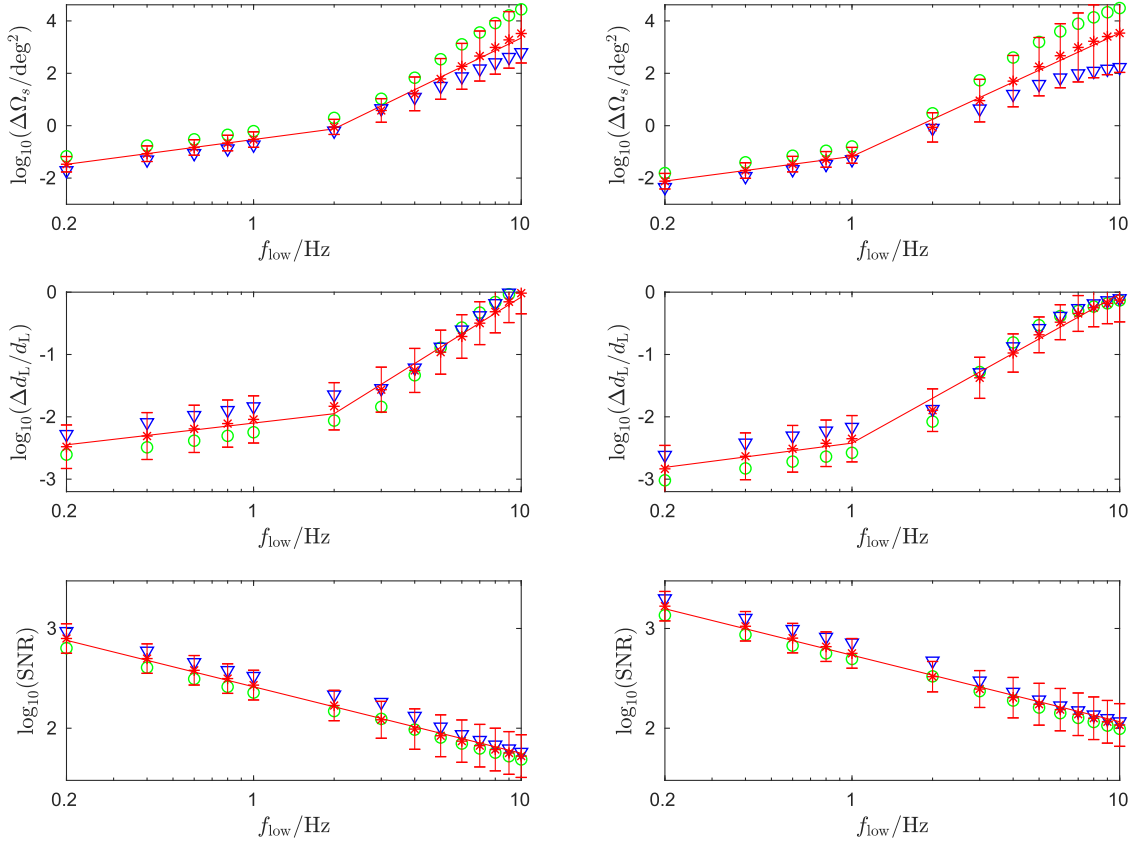


FIG. 8. Angular resolution $\Delta\Omega_s$, distance accuracy $\Delta d_L/d_L$ and SNR as a function of the low-frequency cutoff f_{low} for the ideal experiment. The left panels show the results of BNS sources, and the right panels show the results of NSBH sources. In each panel, the green circles are for a source at $\theta_s = 110.38^\circ, \phi_s = 291.48^\circ, \psi_s = 188.36^\circ, \iota = 75.70^\circ$, and the blue triangles are for a GW source at $\theta_s = 30.37^\circ, \phi_s = 118.05^\circ, \psi_s = 21.45^\circ, \iota = 46.11^\circ$, randomly chosen from 10⁴ samples. The red asterisks and the error bars show the median values and the corresponding standard deviations derived from 10⁴ random samples. Solid red lines are the best-fit broken power-law forms.

$$\log_{10}(\Delta d_L/d_L) = \begin{cases} -2.42 + 0.56(x - x_0), & f \leq 1 \text{ Hz}, \\ -2.42 + 2.39(x - x_0), & f > 1 \text{ Hz}, \end{cases} \quad (23)$$

where $x \equiv \log_{10}(f/\text{Hz})$ and x_0 are the x values at the turning-around point of $f = 2 \text{ Hz}$ and $f = 1 \text{ Hz}$ for BNS and NSBH, respectively. The median values of SNR (Fig. 8, red asterisks) for both sources roughly follow the power-law relation of $\text{SNR} \propto f_{\text{low}}^{-2/3}$ (Fig. 8, red solid line), expected for the binary inspiral signal with a flat noise spectrum density and a constant antenna beam-pattern functions. Results of individual sources (Figs. 8 and 9, green circles and blue triangles) can be observed to deviate slightly from this power-law between 2–10 Hz due to the time dependence of the antenna beam-pattern functions.

Similar dependence of the angular resolution and low-frequency cutoff can be found in ET-D (Fig. 9), where we have used the same samples of BNS and NSBH sources as

for the ideal detector for our investigation. For the BNSs, we can observe a relatively steep change in angular resolution and distance accuracy with the low-frequency cutoff at $f_{\text{low}} > 2 \text{ Hz}$, while the values of SNR change very little. Specifically, for $f_{\text{low}} \gtrsim 3 \text{ Hz}$, the angular resolution can be approximated by the power-law relations of $\Delta\Omega_s \propto f_{\text{low}}^{2.2}$ for BNSs and $\Delta\Omega_s \propto f_{\text{low}}^{1.8}$ for NSBHs. The power-law index is different from that of the ideal detector, due to the frequency dependence of the ET-D sensitivity curve. Consistently, at $f_{\text{low}} \gtrsim 10 \text{ Hz}$, a single detector will have difficulty in localizing GW sources. Note the SNR values in ET-D remain nearly constant for different f_{low} values.

Our results show that in terms of source localization of single 3G detectors, it is worthwhile to extend the detector's sensitivity to frequencies below 10 Hz. For the ET-D type of sensitivity, analyzing data at frequencies lower than 10 Hz could help improve the source localization accuracy even if it does not help increase the SNRs.

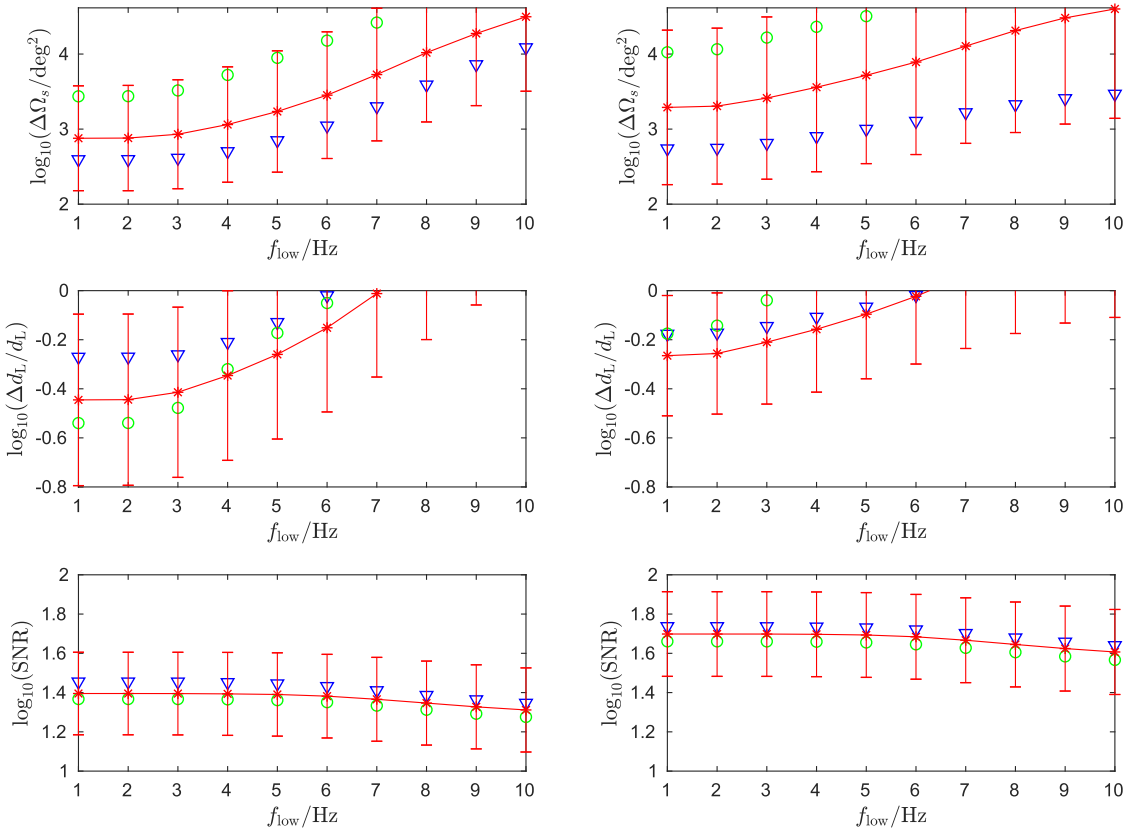


FIG. 9. The same as Fig. 8 but with the ET-D sensitivity for different low-frequency cutoff f_{low} between 1 and 10 Hz.

V. ANGULAR RESOLUTION AND DISTANCE DETERMINATION AS A FUNCTION OF REDSHIFT

We investigate the angular resolution and distance determination of the BNS and NSBH sources at different redshifts for a single 3G detector as well as different networks of up to four 3G detectors. For a comparison of the design of CE with ET-D, seven different 3G network configurations are considered. Specifically, we consider

- (i) **2CE**. Two CE-like detectors, one in the U.S. and one in Europe, at the same site and with same orientation as ET, but with an opening angle of 90° .
- (ii) **CE-ETD**. One CE detector in the U.S., and one ET detector in Europe with the ET-D sensitivity.
- (iii) **2ETD**. Two ET-like detectors with the ET-D sensitivity, one in Europe and one in the U.S., at the same site and with the same orientation as CE, but with an opening angle of 60° .
- (iv) **3CE**. Three CE-like detectors, one in the U.S. and one in Europe, plus one in Australia.
- (v) **3ETD**. Three ET-like detectors with the ET-D sensitivity, one in the U.S. and one in Europe, plus one in Australia.
- (vi) **3cETD**. Three ET-like detectors with ET-D sensitivity, one in the U.S. and one in Europe, plus one in China.

- (vii) **4ETD**. Four ET-like detectors with ET-D sensitivity, one in the U.S., one in Europe, one in China and one in Australia.

The coordinates, orientations, and open angles of the detectors are listed in Table I. We stress that the coordinates and orientations do not represent the actual localizations of the potential detector, and we did not check for the optimal site localizations for 3G networks, which have been well studied in [87]. We use 15,000 simulated random BNS samples of $m_{1,\text{phys}} = m_{2,\text{phys}} = 1.4 M_\odot$ for each redshift values of $z \in [0.1, 2]$ with 0.1 spacing, and for NSBH system of fixed mass pairs of $m_{1,\text{phys}} = 10 M_\odot$ and $m_{2,\text{phys}} = 1.4 M_\odot$ sampled at $z \in [0.1, 2]$ as prescribed in Sec. III.

A. One detector

We consider ET-D for one-detector localization and distance determination of BNS and NSBH sources at different redshifts as it has the best single detector angular resolutions (Sec. IV). The results for the BNS systems are shown in violin plots in Fig. 10 (upper panels), and for the NSBH systems in Fig. 10 (lower panels). We find that for one ET-D detector, the medium angular resolution at $z = 0.1$ for the detected BNS and NSBH sources is around 100 deg^2 and the medium distance accuracy is about 20%. This is already comparable to the localization of the first detected

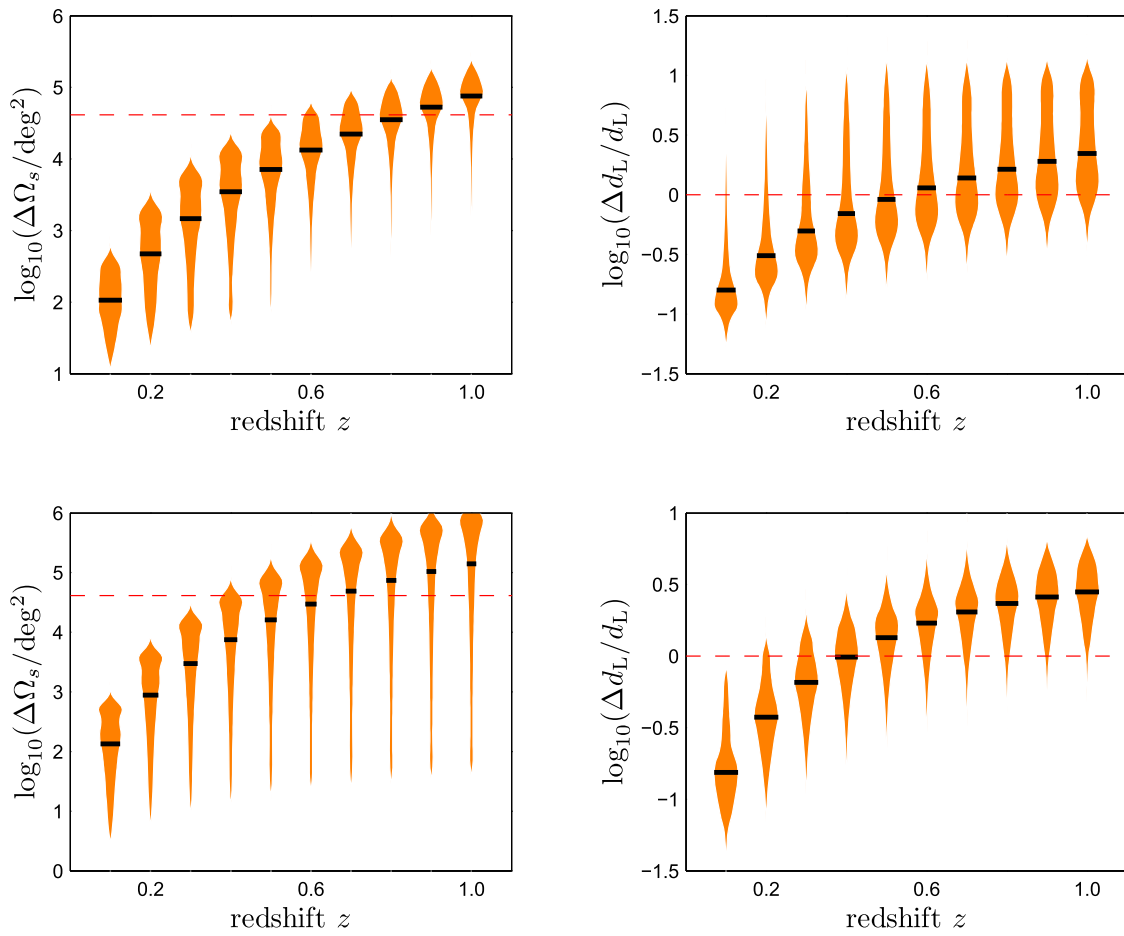


FIG. 10. Violin plots of the angular resolution $\Delta\Omega_s$ (left panels) and distance uncertainties $\Delta d_L/d_L$ (right panels) for the ET-D as a function of redshift z , for BNSs (upper panels) and NSBHs (lower panels). The black bars indicate the median values of the corresponding distribution.

GW event GW150914 by the two Advanced LIGO detectors at O1 sensitivity [1]. At $z = 0.2$, the medium angular resolution is 1000 deg^2 and medium $\Delta d_L/d_L \sim 40\%$.

We have observed a pronounced anticorrelation relation of the distance accuracy with the angular resolution for GW sources for all types of detectors. For one ET-D detector, such anticorrelation relation is shown in Fig. 11 for our BNS samples at $z = 0.1$. The angular resolution of more face-on sources (Fig. 11, right panels, red and blue points) are overall better than more edge-on sources (Fig. 11, right panels, green and yellow points) due to their larger SNRs. On the other hand, the GW polarization for edge-on systems is more linearized and can be better determined by one detector. This together with the time-dependent antenna beam-pattern function helps break its degeneracy with the distance determination. Among those face-on sources, however, the angular resolution is worse for those with a direction perpendicular to the detector plane despite of their larger SNRs. At these directions, the influence of the Earth's rotation is minimum, and therefore the single-detector angular resolution is the worst. Similar conclusion holds for the NSBH sources. Therefore, for a single ET-D like

detector, the face-on sources from the directions parallel to the detector plane have the best angular resolution, while the edge-on sources have overall better distance determination.

In comparison, we replace ET-D with the ideal detector that has a better low-frequency sensitivity than ET-D (Fig. 1) and perform the same calculations also for 15,000 random samples of BNSs and NSBHs. We found that for both BNSs and NSBHs, we have an order of magnitude improvement in the angular resolution and a factor of a few improvement in distance determination (See Fig. 12). Specifically, at $z = 0.1$ the medium angular resolution is $\sim 10 \text{ deg}^2$ and medium $\Delta d_L/d_L \sim 4\%$, while at $z = 0.3$ the medium $\Delta\Omega_s \sim 100 \text{ deg}^2$ and medium $\Delta d_L/d_L \sim 15\%$. For both ET-D and the ideal detector, we find that the angular resolutions and distance determinations of NSBHs are slightly worse than that of BNSs, since the effect of the Earth's rotation is weaker for NSBHs.

B. Network of two detectors

The result for the 2CE network can be found in Fig. 13. At $z = 0.1$, the medium $\Delta\Omega_s$ is around a few square-degrees,

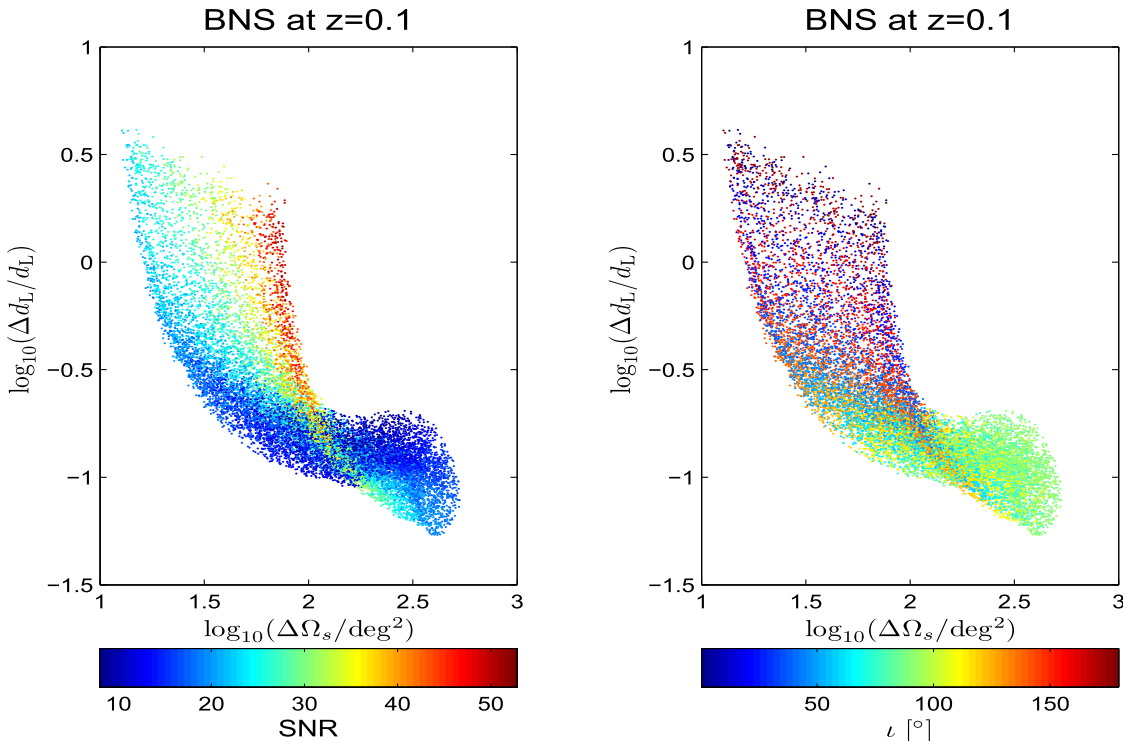


FIG. 11. The distributions of $\Delta d_L/d_L$ with respective to $\Delta\Omega_s$ for 15,000 BNS samples at redshift $z = 0.1$. The figure shows the results of ET detector located at Europe with ET-D noise. In the left panel, the color indicates the SNR value of the sample, and in the right panel it indicates the inclination angle ι .

and medium $\Delta d_L/d_L$ is a few percent for BNSs (Fig. 13, upper panels) and similarly for NSBHs (Fig. 13, lower panels). The medium angular resolution at $z = 0.2$ is about 20 deg^2 and medium distance accuracy $\sim 50\%$. On the other hand, there is a small but noticeable fraction of BNS and NSBH sources that can be localized to sub-square degree accuracy at $z < 0.3$, and with distance accuracy to be less than 10% at $z = 0.1$. Even for the sources at $z = 2$, there is still a small but noticeable fraction of sources that can have angular resolution to be within $\Delta\Omega_s \sim 10 \text{ deg}^2$. As the effect of the Earth rotation is nearly negligible for the CE detector, these are mainly due to the much larger SNRs from the superior sensitivity of the CE detectors, especially for those face-on binaries. Note also, the fraction of BNSs detected by the two CE detectors is also much more than the two ET-D detectors (Fig. 19).

The medium angular resolution will be greatly improved for sources at high- z when the two-detector network include at least one ET-D due to its low-frequency sensitivities as discussed previously. In comparison with the 2CE network at the same locations, we find a medium angular resolution of a few degrees at $z = 0.1$, 15 deg^2 at $z \sim 0.2$, and $\sim 100 \text{ deg}^2$ at $z = 2$ for the CE-ETD network. The improvement in distance accuracy is also a factor of a few better than the 2CE network. However, the fraction of sources with superior localization observed with the 2CE network is reduced.

If both detectors are of the ET-D type, nearly all the BNS sources at $z < 0.2$ can be localized within 10 deg^2 (Fig. 15). The medium angular resolution for the BNS sources is $\lesssim 1 \text{ deg}^2$ at $z = 0.1$ (Fig. 15, left panels), and 10 deg^2 at $z = 0.4$. The medium angular resolution for NSBH sources is slightly worse. It is around 10 deg^2 at $z = 0.3$. The 10% medium distance uncertainty can be achieved at $z = 0.3$ for both the BNS and NSBH sources (Fig 15, right panels).

In Fig. 16, we present the two-dimensional $\Delta\Omega_s - \Delta d_L/d_L$ scatter plot of BNS samples at $z = 0.1$ detected by the 2ETD network. Similar to the single-detector case in Fig. 11, there is a pronounced anticorrelation between the angular resolution and distance accuracy. Similarly, the face-on binaries have overall better angular resolution and SNRs, but worse distance accuracy. In the meanwhile, the edge-on binaries have a better distance determination, but worse angular resolution and SNRs. We can also confirm that the anticorrelation relation holds for both BNSs and NSBHs at any given redshift. Note the relation of angular resolution and the GW direction relative to the detector plane is no longer obvious as the baseline effect dominates for a network of detectors.

In summary, we can conclude the following: (1) For the network consisting of only CE-like detectors, accurate localization can be achieved mainly for nearby sources with 100 deg^2 medium angular resolution achieved at $z = 0.5$.

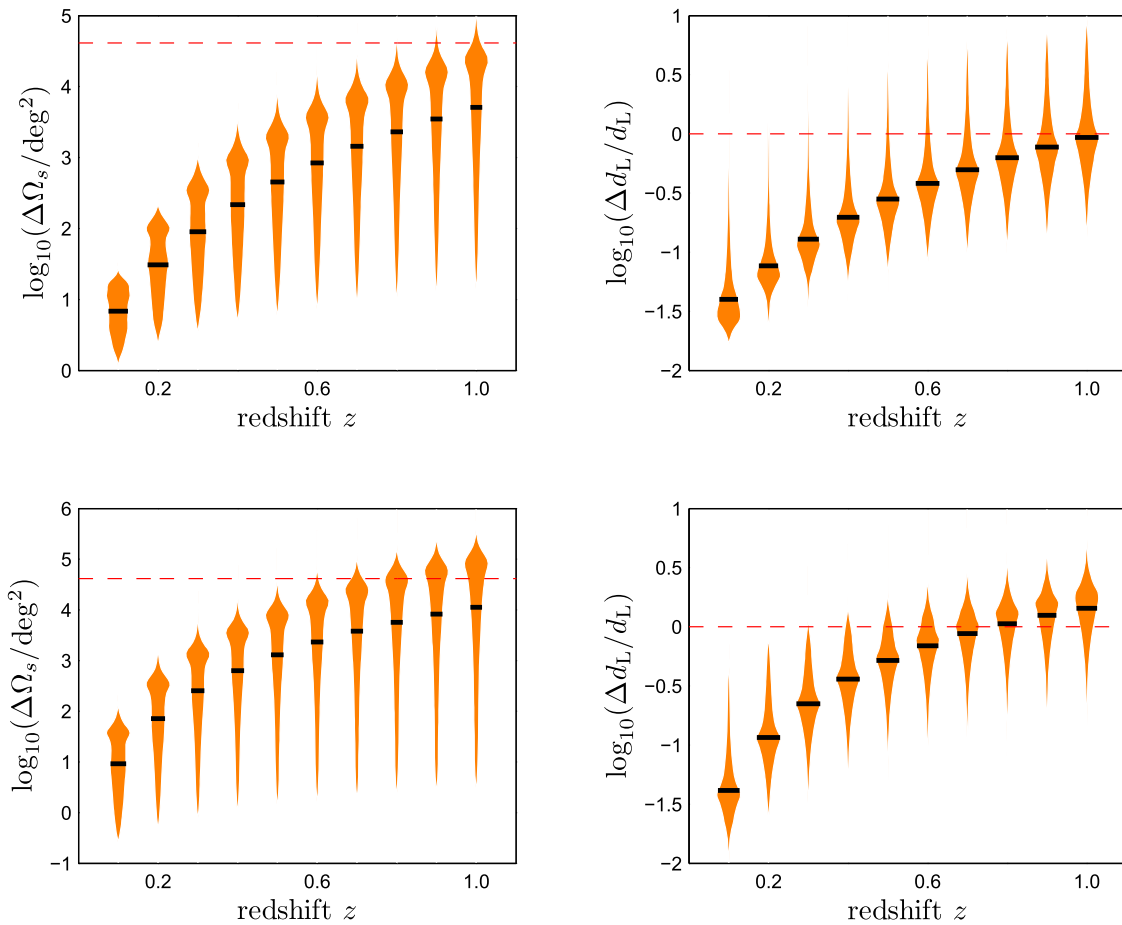


FIG. 12. Same as Fig. 10, but ET-D noise is replaced by the ideal noise described in Fig. 1 with low-frequency cutoff $f_{\text{low}} = 5$ Hz.

However, due to the superior sensitivity of the CE detector, the total number of sources with superior localization at low-redshift might be comparable to that of the 2ETD network. (2) For CE-ETD and 2ETD networks, the accurate localization can be greatly extended to high redshift $z \sim 2$, where we have $\Delta\Omega_s \sim 100$ deg 2 for most BNSs and NSBHs. In particular for the nearest sources detected by 2ETD network at $z = 0.1$, the localization can be as accurate as $\Delta\Omega_s \sim 1$ deg 2 and $\Delta d_L/d_L \sim 5\%$ for most sources. (3) We observe again that for binary coalescences at a fixed redshift, the face-on binaries can be detected with a better angular resolution, while the edge-on binaries with a better luminosity distance accuracy.

C. Networks of three and four detectors

The benefits of building a large network of GW detectors including Australia and China have been widely discussed [32,88,89]. The advantages of multidetector networks for the localization of GW sources have been studied in a previous work [32] for BBHs with component masses larger than $12 M_\odot$. In this paper, we focus instead on binaries with small masses, i.e. BNSs and NSBHs that have significantly long-duration signals in the frequency band of 3G detectors.

The angular resolution and distance accuracy for the 3CE network are shown in Fig. 17 for both BNSs and NSBHs in the redshift range $z \in [0.1, 2]$. Compared with the results of 2CE network in Fig. 13, we find that a 3CE network can greatly improve the localization accuracy for binary coalescences at any redshift. At $z = 0.1$, we have $\Delta\Omega_s \in (0.005, 0.6)$ deg 2 and $\Delta d_L/d_L \in (0.006, 0.25)$ for BNSs, $\Delta\Omega_s \in (0.02, 0.5)$ deg 2 and $\Delta d_L/d_L \in (0.01, 0.25)$ for NSBHs. At $z = 1$, we have $\Delta\Omega_s \in (0.3, 30)$ deg 2 and $\Delta d_L/d_L \in (0.03, 1)$ for BNSs, $\Delta\Omega_s \in (0.3, 50)$ deg 2 and $\Delta d_L/d_L \in (0.03, 1)$ for NSBHs. At $z = 2$, we still have $\Delta\Omega_s \in (2, 100)$ deg 2 for both BNSs and NSBHs, while the medium $\Delta d_L/d_L = 30\%$ for BNSs and medium $\Delta d_L/d_L = 20\%$ for NSBHs.

Figure 18 shows the results for the 3ETD network. Compared with the 3CE network, we find that this network gives similar, but slightly narrower distributions, for the localization of GW sources at all redshifts. In Fig. 19, we plot the fraction of detectable BNS and NSBH sources as a function of redshift z for various networks. Thanks to the lower noise level, the 3CE network has much better detection rates at high redshift $z > 0.5$ than all other detector networks in consideration. For instance, at $z = 2$, the 3CE network can

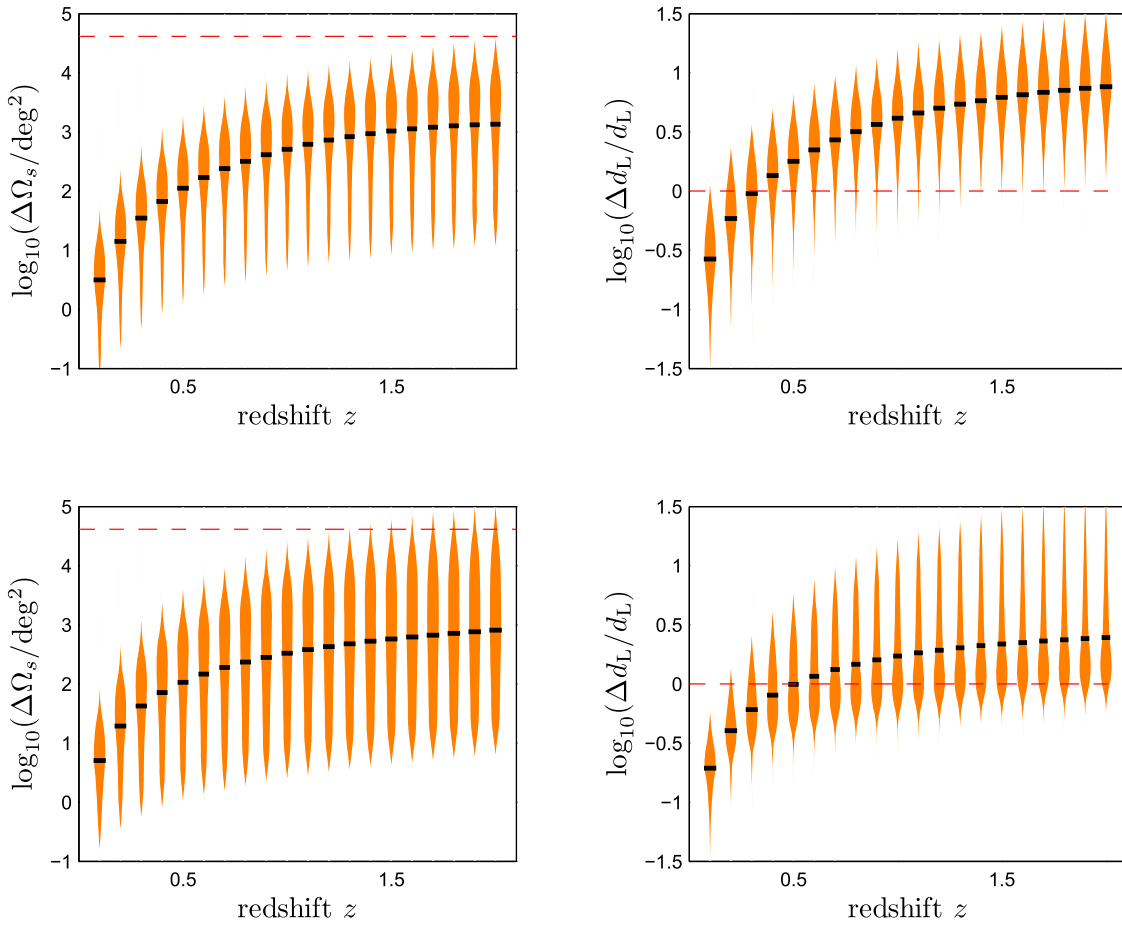


FIG. 13. Same as Fig. 10, but for the 2CE network.

detect 90% BNSs and 98% NSBHs, while the 3ETD network detects only 38% BNSs and 74% NSBHs.

For the 4ETD network (See Fig. 20), we find that the localization accuracies of binary coalescences are slightly better than that for the three-detector networks. For BNSs, the angular resolution $\Delta\Omega_s$ can be improved by a factor ~ 2 , and $\Delta d_L/d_L$ shows no significant improvement. For the NSBHs, we find the medium values of both $\Delta\Omega_s$ and $\Delta d_L/d_L$ have no significant improvement, from that of the three-detector networks at any redshift. However, the spreads of the distributions of $\Delta\Omega_s$ for 4ETD network are much narrows than the three-detector networks. For instance, for the BNSs at $z < 0.1$, we find most sources can have a localization accuracy of $\Delta\Omega \in (0.01, 0.1) \text{ deg}^2$, which is significantly smaller to directly identify their host galaxies. Even for the BNSs at $z = 2$, we also have $\Delta\Omega \in (2, 10) \text{ deg}^2$, which is helpful for follow-up observations on their EM counterparts.

From Figs. 21 and 22, we again find a significant anticorrelation between $\Delta\Omega_s$ and $\Delta d_L/d_L$ for BNSs at $z = 0.1$, similar to the cases of a single ET-D detector and of the 2ETD network. The face-on GW sources have a better angular resolution, while the edge-on sources have a better distance determination. For 3G GW detectors,

regardless an individual detector or detector networks, it seems impossible to have both the best angular resolution and the best distance determination at the same time. However, as long as there are more than one detector, there is always a positive correlation between the angular resolution and SNR.

D. Effect of a larger network

The angular resolution of a GW source detected by detector networks depends not only on the area of the errors $\Delta\Omega_s$, but also on the two-dimensional shapes of error ellipses in the two sky directions. For the three 2-detector networks considered, we show in Fig. 23 the sky maps of the error ellipses of angular parameters derived for the BNSs at the redshift $z = 2$. In the left panels, for each sample, we adopt $\iota = 0^\circ$, i.e., the face-on sources, while in right panels $\iota = 45^\circ$ for comparison. For face-on sources, which have the most accurate medium angular resolutions among all the sources at same redshift, we find that 2CE network gives the best localization accuracy. For the networks consisting of one or two ET-Ds, the angular resolution of the face-on sources are slightly worse, due to lower SNRs. These results are consistent with those in violin plots in Figs. 13, 14, and 15. However, for sources

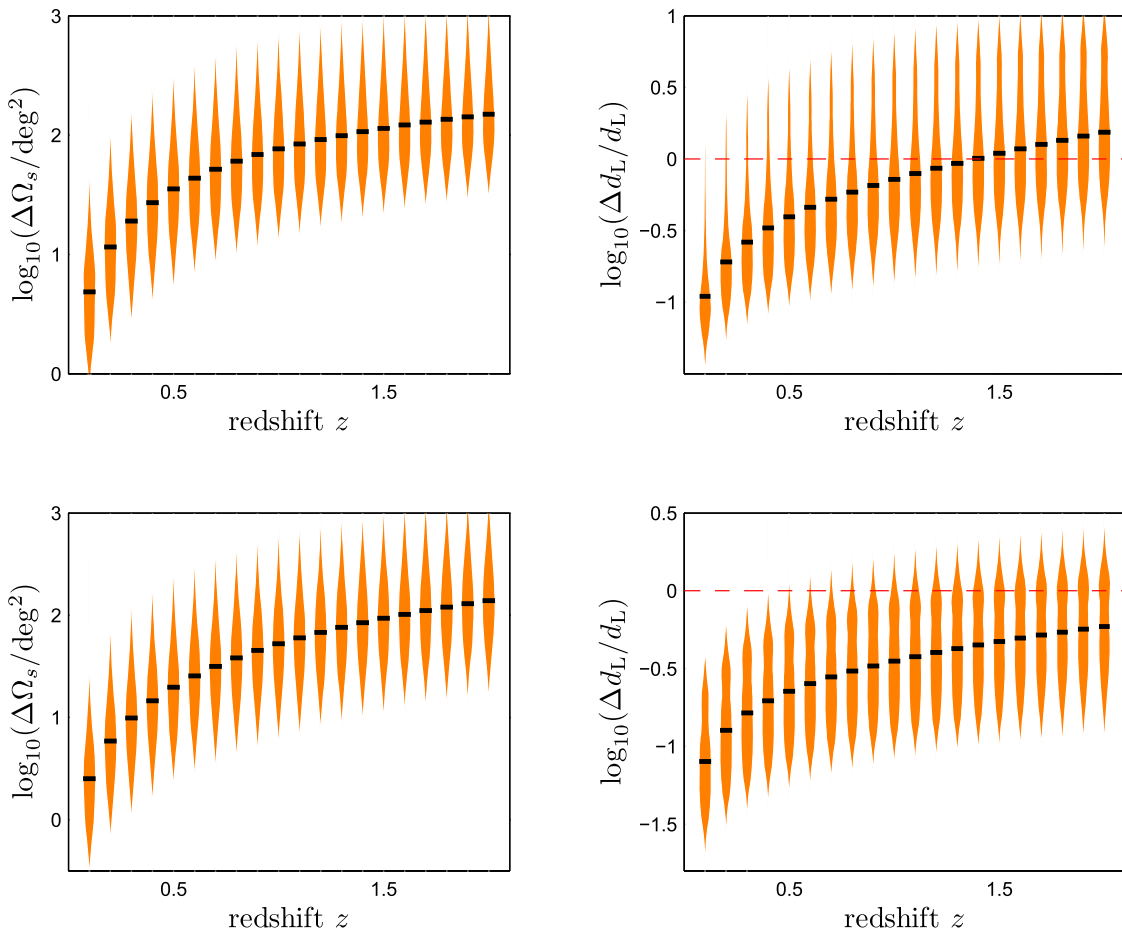


FIG. 14. Same as Fig. 13, but for the CE-ETD network.

with general inclination angles, from right panels of Fig. 23, we find that 2ETD and CE-ETD networks always achieve much more accurate medium angular resolution. For these two-detector networks, we also find that in most region of sky, the error ellipses are string-shaped as it is mostly determined by the arrival time delay of GWs between two detectors. This is similar to the localization of the GW events GW150914, as well as GW151226 and GW170104, observed by two Advanced LIGO detectors [1,4,5]. The shapes of the error ellipses strongly depend on the positions of the GW sources in the sky, as well as locations of detectors. However, the far more superior single-detector angular resolution of ET-D helps remove some of the extremely long ellipses in the sky map of the 2ETD network, which is similar to the localization of the GW event GW170814, observed by the collaboration of two Advanced LIGO detectors and one Advanced Virgo detector [7]. These features also hold for the NSBH sources.

For the BNS sources at $z = 2$, we show in Fig. 24 the sky maps of the error ellipses of sky directions for three-detector and four-detector networks. Comparing with the results of two-detector networks, we find that the error ellipses are less elongated as expected from the contribution from more than

one set of long baselines between detectors for these multidetector networks. The 3ETD network and 3cETD network show similar results for binaries with different inclination angles. One noticeable difference is that, the orientation of the error ellipses at a given sky direction is different for different networks, which depends on the detector's sites on the Earth. In addition, for the four-detector network, consisting of detectors in Europe, U.S., Australia, and China, we find the localization of detector network becomes isotropic for binary coalescences from all sky directions. This means that increasing the detector number can help significantly remove observational blind regions in the sky.

VI. IMPLICATION FOR COSMOLOGY

As shown in previous sections, from the GW signal itself one can measure the luminosity distance of the binary coalescences independently without having to rely on a cosmic distance ladder. If the redshift of the GW sources could also be measured by other means, such as by observing their EM counterpart or identifying the host galaxies, these GW sources can be used as *standard sirens*, and $d_L - z$ relation can be used to study the evolution

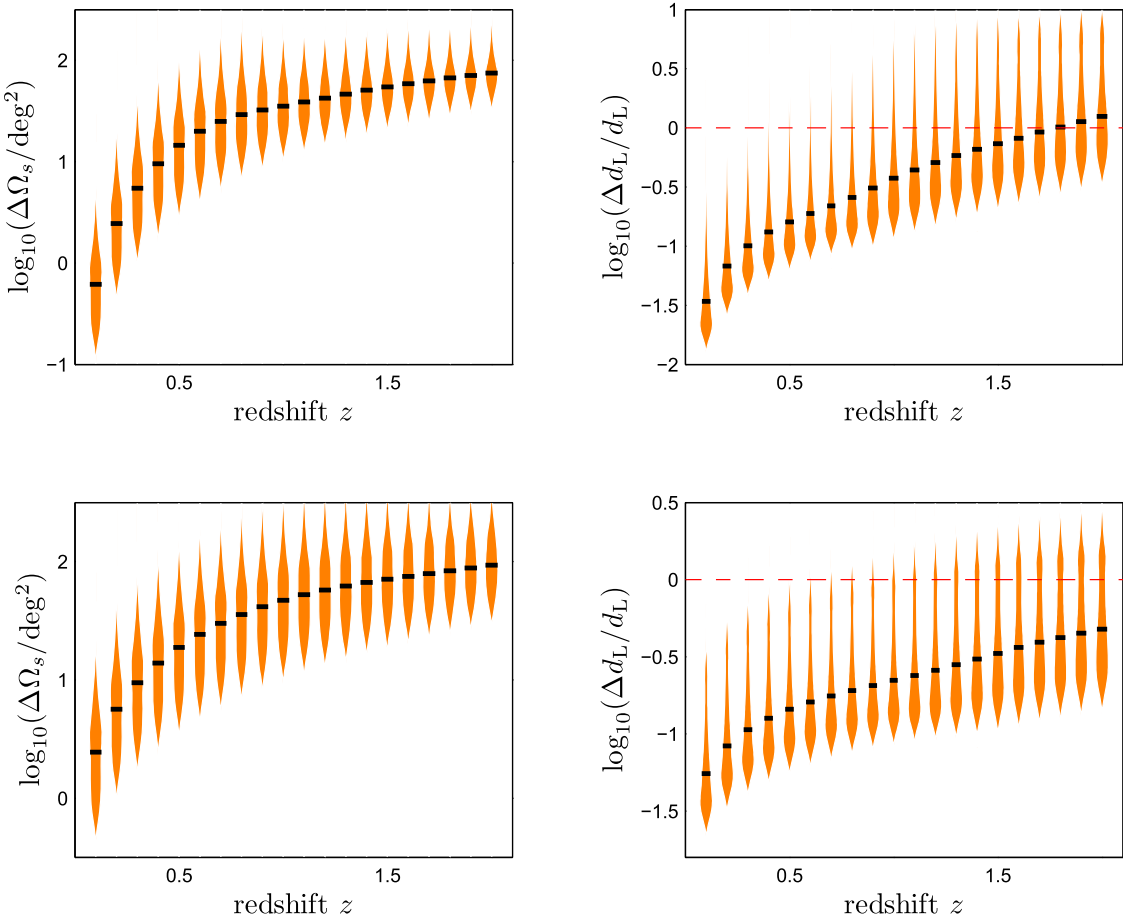


FIG. 15. Same as Fig. 13, but for the 2ETD network.

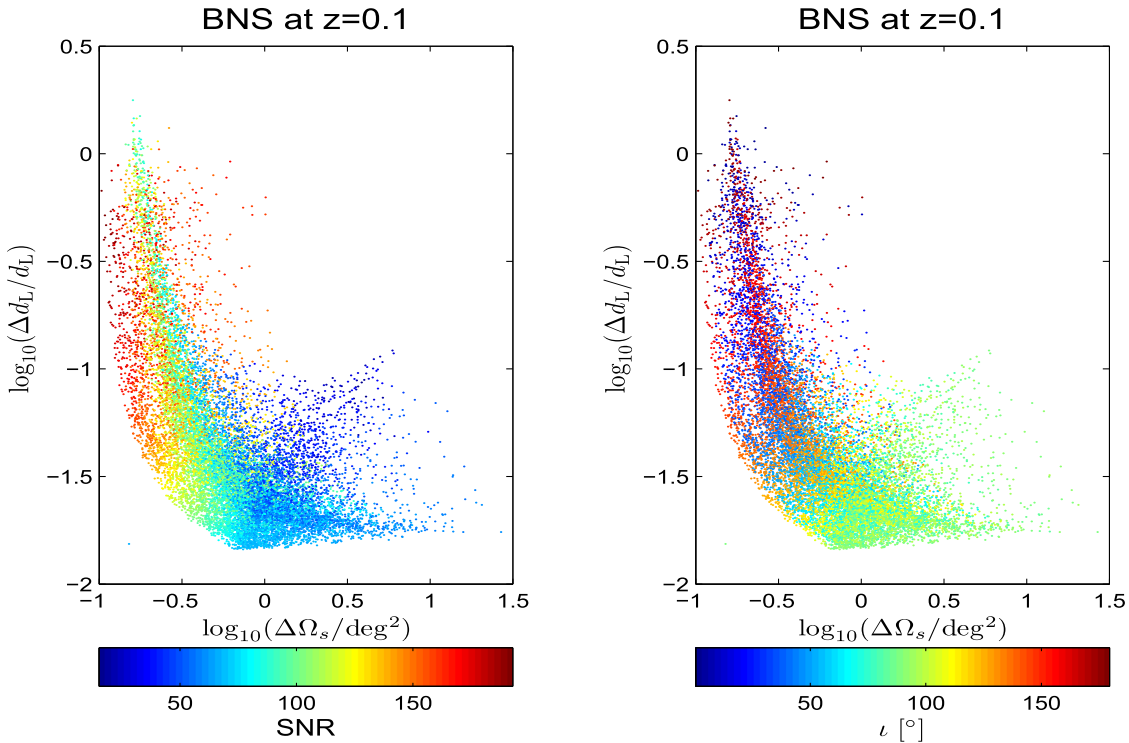


FIG. 16. Same as Fig. 11, but a single ET-D detector is replaced by the 2ETD network.

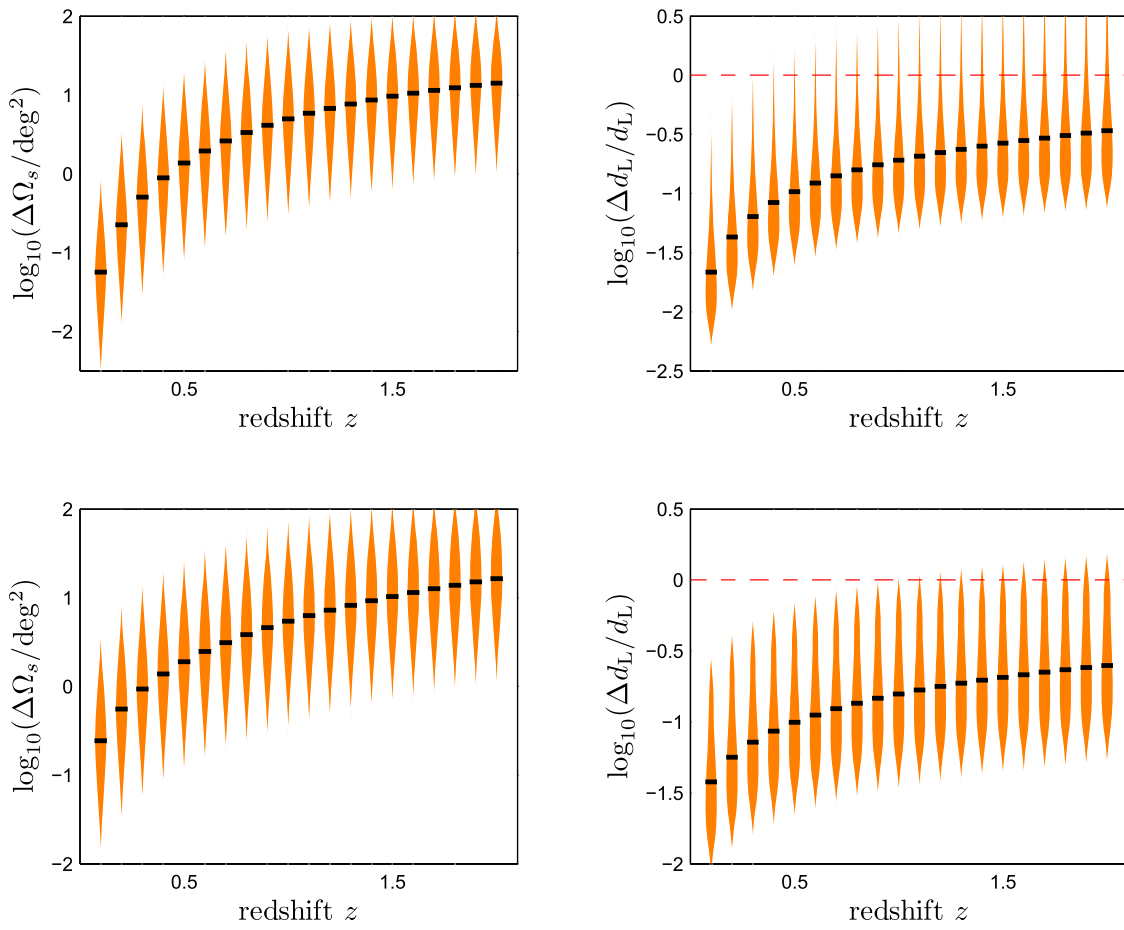


FIG. 17. Same as Fig. 13, but for the 3CE network.

history of the Universe [37]. With the 2G detector network, the GW standard sirens at low redshift have been applied to measure the Hubble constant [38]. If the high redshift GW signals can be observed by 3G ground-based detectors [21,22,24], space-based LISA [39–42], BBO or DECIGO [43], these sources are useful to determine the EoS of dark energy. In this section, based on the GW source localization of 3G detector networks, we consider the constraint on the Hubble constant H_0 , the deceleration parameter q_0 , and the EoS of cosmic dark energy by the inspiraling BNSs and NSBHs.

A. Determination of Hubble constant

In the Friedmann-Lemaître-Robertson-Walker (FLRW) universe, if $z \ll 1$, the luminosity distance and the redshift satisfy the Hubble's law, which reads $d_L = z/H_0$, where H_0 is the Hubble constant. The current Hubble constant is $H_0 = 67.8 \pm 0.9 \text{ km s}^{-1} \text{ Mpc}^{-1}$, derived from the cosmic microwave background (CMB) radiation data [82]. Meanwhile, the large-scale structure observations inferred a different value $H_0 = 73.24 \pm 1.74 \text{ km s}^{-1} \text{ Mpc}^{-1}$ [90], which conflicts with the CMB result at more than 3σ confidence level. The tension of measured H_0 value derived

from different observations is one of the crucial puzzles of modern cosmology. On the other hand, observing GWs from binary coalescences at low-redshift can help determine the sources' luminosity distance at reasonably high precisions. The redshifts of these events can possibly be obtained with many methods. One possible way is to observe their EM counterparts, for instance, BNS and NSBH are hypothesized to be accompanied by short-hard GRBs or kilonova emissions, or to identify their host galaxies through their excellent position resolutions. Some other methods are also proposed, such as by detecting the contributions to the GW phases caused by tidal effects [91], by assuming a narrow mass distribution of NSs [92], by using the signature encoded in the post-merge signal [93], or by directly observing the cosmological phase drift of a single GW source [94]. In this paper, we bypass the details and assume that one of the methods can be used to obtain the redshift information. For instance, combining with the observations of its EM counterpart, the GW data from the recently detected BNS event GW170817 has already been used to place an interesting constraint on H_0 with $H_0 = 70.0^{+12.0}_{-8.0} \text{ km s}^{-1} \text{ Mpc}^{-1}$ [95], which is consistent with the results derived from both CMB and SNIa data.

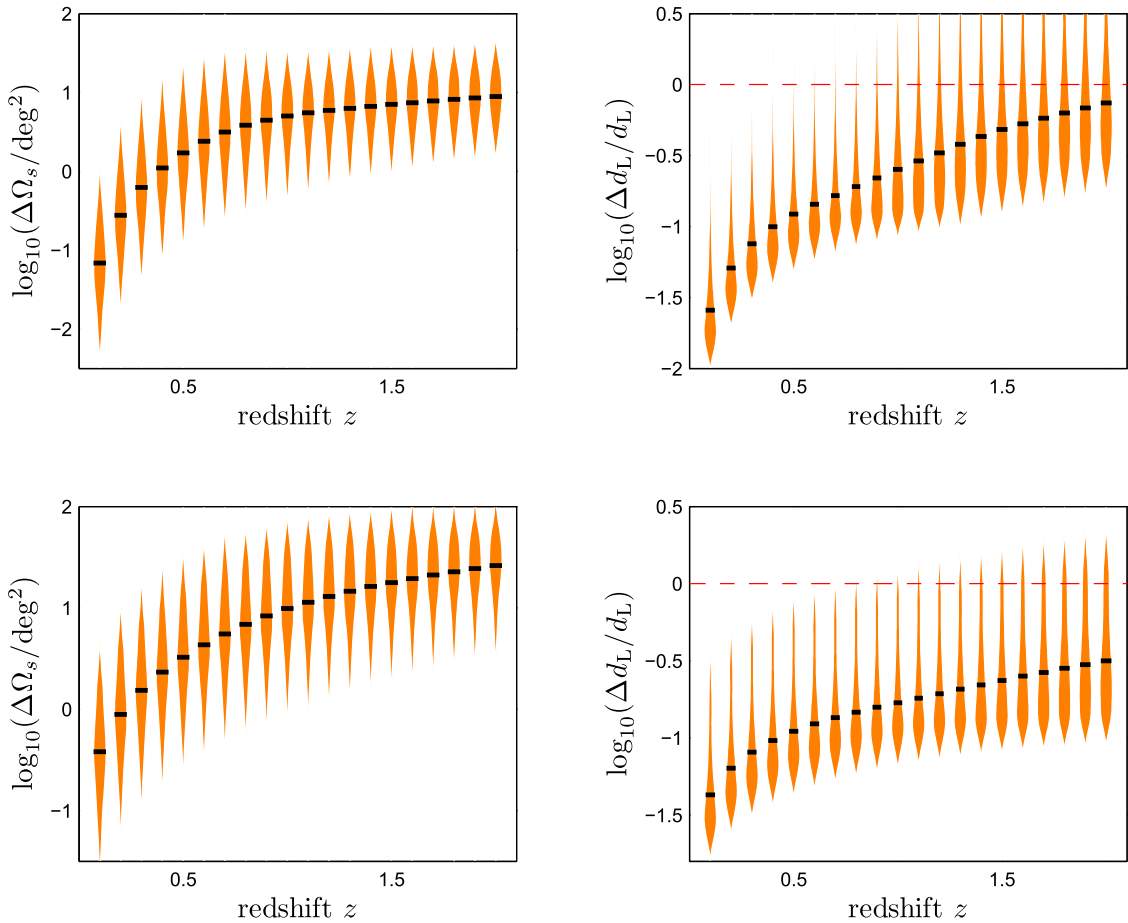
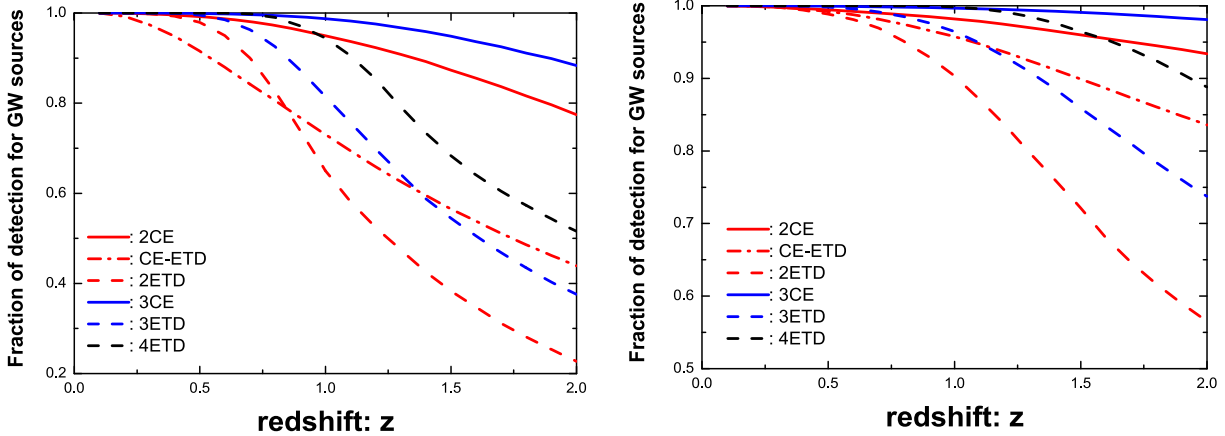


FIG. 18. Same as Fig. 13, but for the 3ETD network.

FIG. 19. For various detector networks, the fraction of detectable GW sources (i.e. $\rho > 8$) as a function of redshift z . The left panel shows the results of BNSs and the right one is for NSBHs.

For simplification, we consider only the nearby GW sources, i.e. BNSs or NSBHs, at $z = 0.1$. However, not all the binaries in this redshift can be used to constrain H_0 . We select the sources with criteria of $\text{SNR} \geq 8$ and $\Delta d_L/d_L \leq 0.5$. The fraction of effective samples is given by $f_{H_0} = N_{\text{eff}}/N_{\text{tot}}$, where N_{eff} is the number of the

effective samples that satisfy the selection criteria, and N_{tot} is the total simulated samples considered. We simulate $N_{\text{tot}} = 10^5$ samples at $z = 0.1$ with random sky directions, inclination angles and polarization angles, and calculate the values of f_{H_0} for various detector networks. The results are listed in Tables II and III and Fig. 25. We find that for the

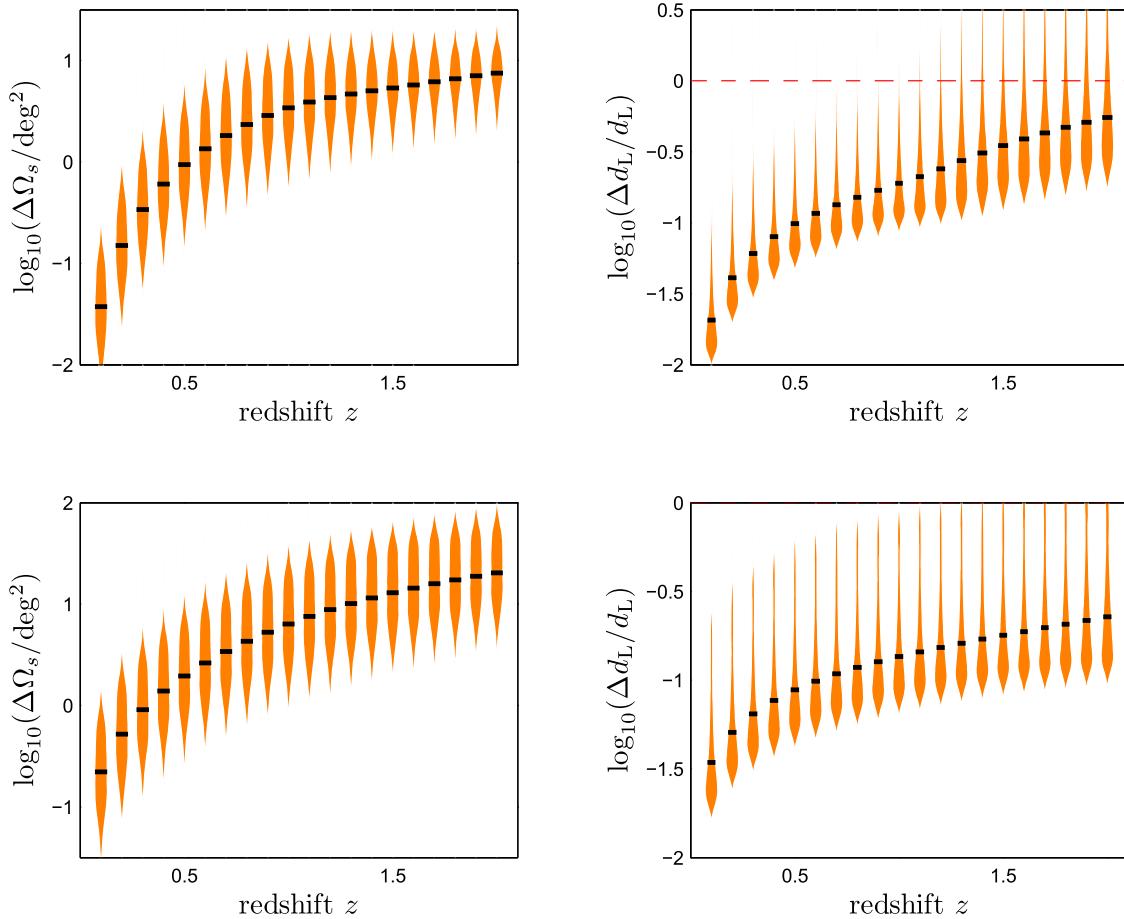


FIG. 20. Same as Fig. 13, but for the 4ETD network.

3G networks, nearly all the samples at $z = 0.1$ satisfy the criteria, regardless of the detector types or network configurations.

For a set of inspiral events with known redshift, the uncertainty of H_0 can be estimated by the following formula

$$\frac{\Delta H_0}{H_0} = \left\{ \sum_k \left(\frac{\Delta d_L}{d_L} \right)_k^{-2} \right\}^{-1/2}, \quad (24)$$

where $k = 1, 2, 3, \dots, N$, represents the k -th selected GW event. The quantity $(\Delta d_L/d_L)_k$ is the uncertainty of distance of the k -th source. We have ignored in Eq. (24) the photometric redshift errors and the possible errors generated by the peculiar velocities of the sources relative to the Hubble flow [96]. When the number of the selected GW events is large, Eq. (24) can be replaced by the following form:

$$\frac{\Delta H_0}{H_0} = \frac{A_{H_0}}{\sqrt{N}}. \quad (25)$$

Note that, the total number of the effective GW events N should be assumed in our calculation. The coefficient $A_{H_0}^{-2}$ is

the average of $1/(\Delta d_L/d_L(\hat{\gamma}))^2$ over the angles $\hat{\gamma} = (\theta_s, \phi_s, \iota, \psi_s)$, that is

$$A_{H_0}^{-2} = \left\langle \frac{1}{(\Delta d_L/d_L(\hat{\gamma}))^2} \right\rangle_{\hat{\gamma}}. \quad (26)$$

In order to evaluate A_{H_0} , we utilize all the effective samples, selected from 10^5 random samples as mentioned above. The results of various detector networks are listed in Tables II and III for BNSs and NSBHs, respectively.

For the BNSs, Table II shows that the 2CE and CE-ETD networks give the similar constrains: $\Delta H_0/H_0 \simeq 1.3\%$ could be achieved if 40 sources are selected, which is comparable to the current accuracy. For the 2ETD network, three-detector, or four-detector networks, the constraint on H_0 becomes much more stringent, with $\Delta H_0/H_0$ around four times smaller. For these networks, a total of 10 selected sources can already achieve $\Delta H_0/H_0 \simeq 0.6\%$, which is two times smaller than the best constraint on H_0 available at this writing. In comparison with BNSs, NSBHs always yield slightly worse constraint on H_0 , except for the CE-ETD network where the results are better. Note the best constraint of H_0 is mainly contributed by the GW sources with

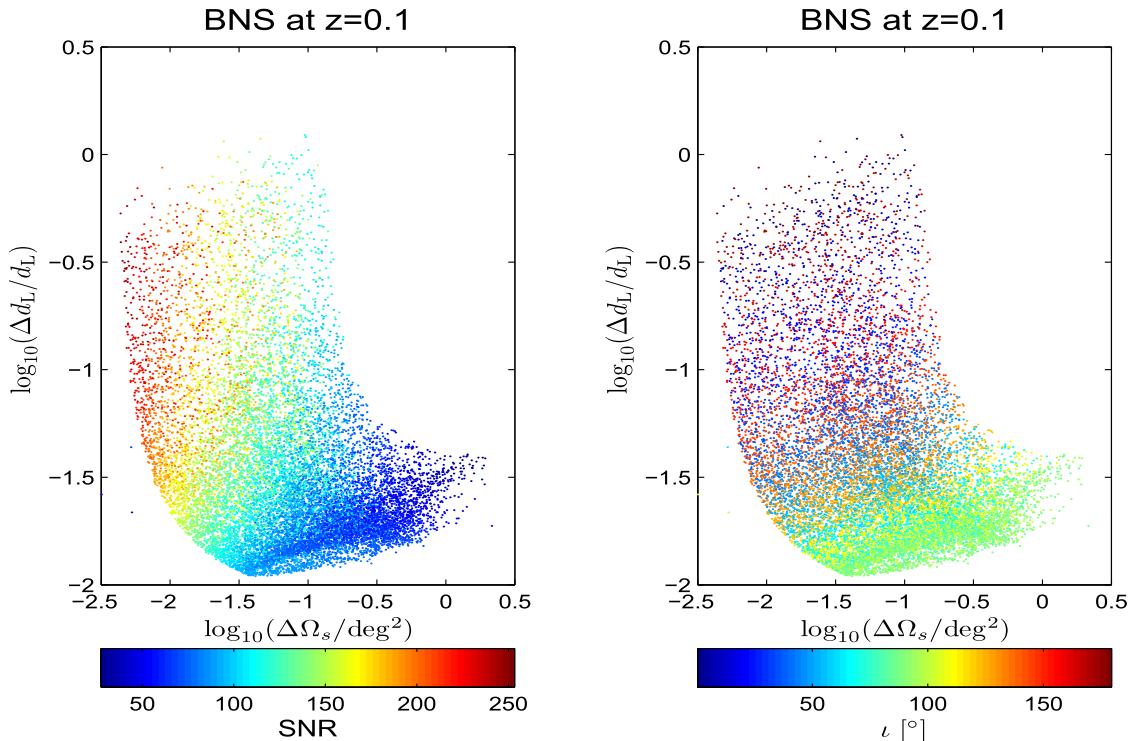


FIG. 21. Same as Fig. 11, but the single ET-D detector is replaced by the 3ETD network.

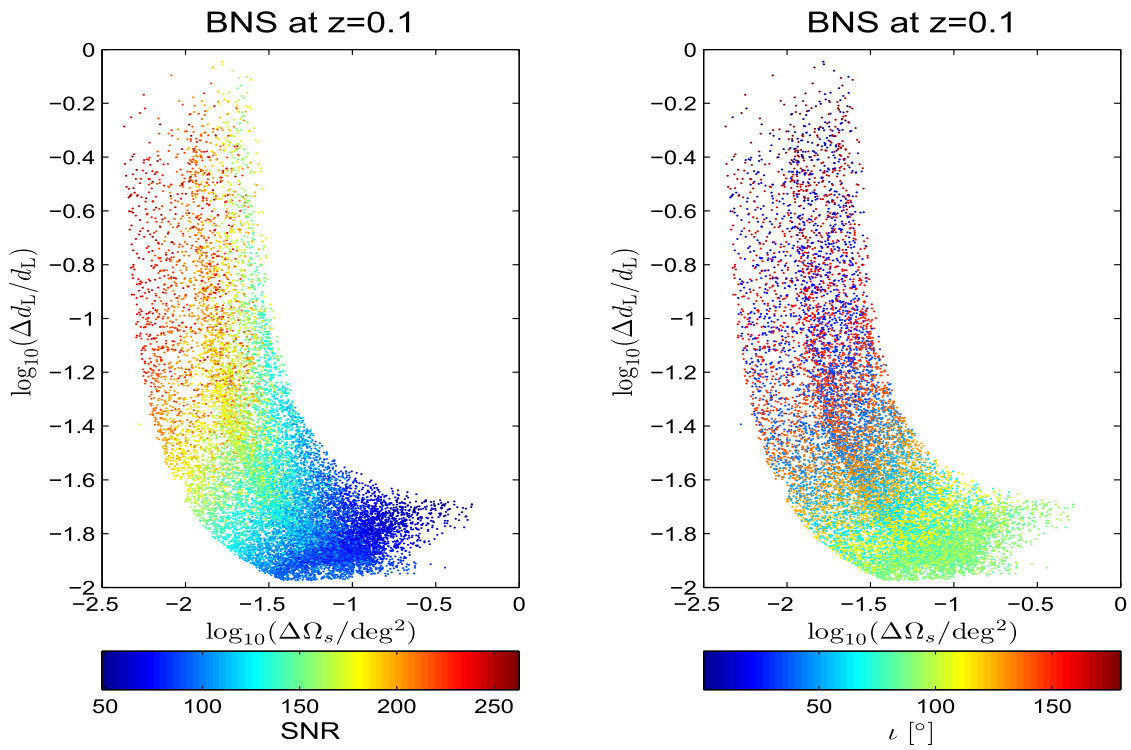


FIG. 22. Same as Fig. 11, but the single ET-D detector is replaced by the 4ETD network.

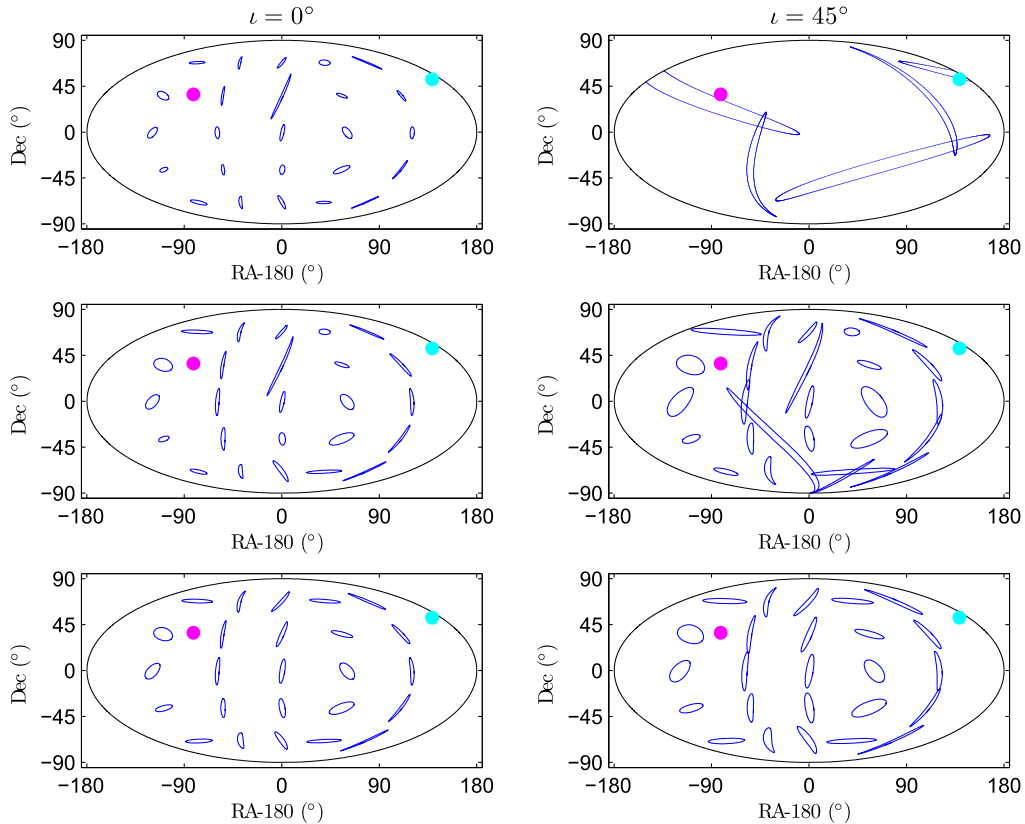


FIG. 23. For the BNSs at $z = 2$, in equatorial coordinate system, this figure shows all-sky map of error ellipses of angular parameters for two-detector networks of 2CE (upper panels), CE-ETD (middle panels), 2ETD (lower panels). The left panels show the results of face-on sources, and the right panels show that with the inclination angle $\iota = 45^\circ$. In each panel, the magenta dot denotes the location of European detector at $t = 0$ in equatorial coordinate, the cyan dot denotes that of American detector.

the best distance determination, i.e. the edge-on binaries, instead of the face-on ones.

B. Determination of deceleration parameter

The deceleration parameter q_0 in cosmology is a dimensionless measure of the cosmic acceleration of the expansion of space in an FLRW universe. It is defined as $q_0 \equiv -\frac{\dot{a}a}{\dot{a}^2}|_{t=t_0}$, where a is the scale factor of the universe and the dots indicate derivatives by the proper time t with t_0 representing the present time. A measurement of a negative q_0 indicates the accelerating expansion of the Universe at the present time. In the flat Λ CDM model, q_0 is directly related to the effective EoS of the universe w by the relation $q_0 = \frac{3}{2}(1 + 3w)$, or equivalently it is related to the matter density parameter Ω_m by the relation $q_0 = \frac{3}{2}\Omega_m - 1$. Latest observations give $\Omega_m = 0.308 \pm 0.012$ [82], which means $q_0 = -0.538 \pm 0.018$, and strongly supports the accelerating expansion model of the Universe.

We investigate the potential constraint of q_0 by detected GW events at redshift $z < 2$, through the observations of the 3G detector networks. For a flat Λ CDM model, q_0 , or equivalently Ω_m , is related to the luminosity distance d_L by [97],

$$d_L(z) = \frac{1+z}{H_0} \int_0^z \frac{dz'}{\sqrt{\Omega_m(1+z')^3 + (1-\Omega_m)}}, \quad (27)$$

which depends on both H_0 and Ω_m (or, equivalently q_0). In this subsection, we assume that the Hubble constant H_0 is already well measured, either by other cosmological observations, such as the CMB observations [82], or by the observations of the nearby GW events as discussed in the last section, where H_0 can be measured with unprecedented accuracy. Thus, assuming that the redshifts are known, the accuracy of measuring q_0 using these binary events depends solely on the uncertainties in measuring their luminosity distance d_L . Specifically, the uncertainty of q_0 can be estimated by the formula

$$\Delta q_0 = \left\{ \sum_k \left(\frac{\partial \ln d_L / \partial q_0}{\delta d_L / d_L} \right)_k^2 \right\}^{-1/2}, \quad (28)$$

where the values of $\partial \ln d_L / \partial q_0$ are numerically calculated. For the high- z GW events, distance measurements are subject to two kinds of uncertainties: the statistical error $\Delta d_L / d_L$ which can be estimated using a Fisher matrix as discussed above, and an additional error due to

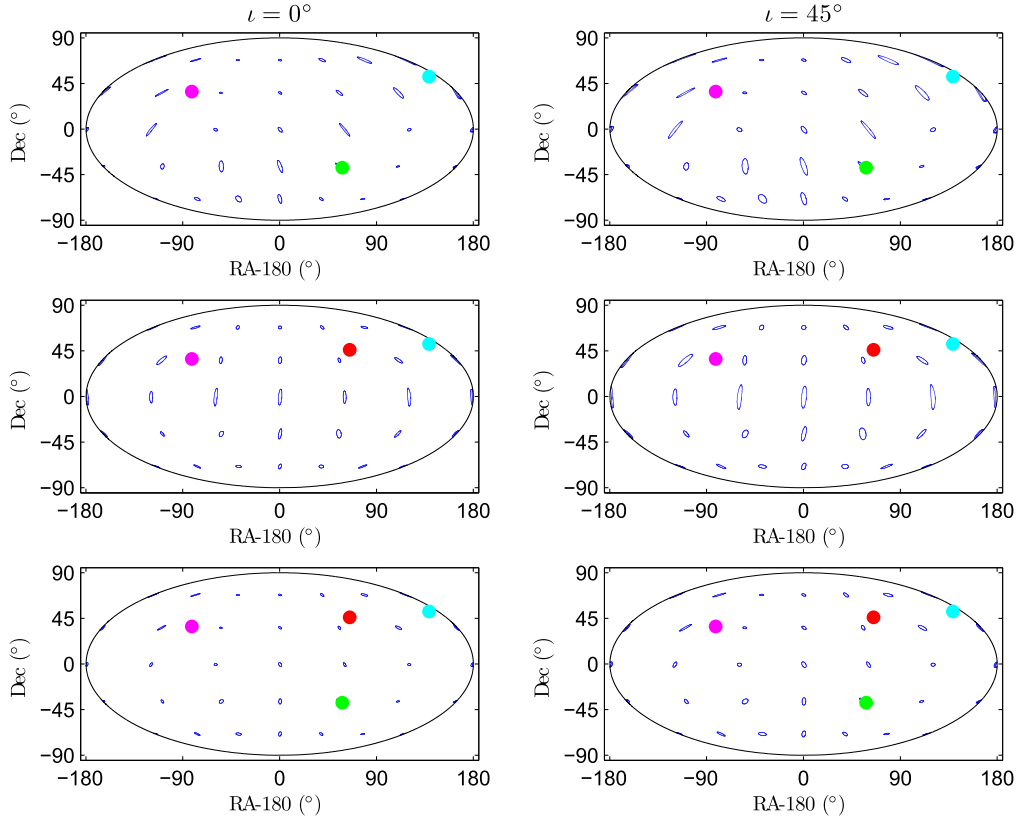


FIG. 24. Same as Fig. 23, but for the results of detector networks 3ETD (upper panels), 3cETD (middle panels) and 4ETD (lower panels). In each panel, the magenta dot denotes the location of European detector at $t = 0$ in equatorial coordinate, the cyan dot denotes that of American detector, the green dot denotes that of Australian detector, and the red dot denotes that of Chinese detector.

the effects of weak lensing.⁶ Following previous works in [21,22], we assume the contribution to the distance error from weak lensing follows the relation $\tilde{\Delta}d_L/d_L = 0.05z$, and that the total uncertainty of d_L is taken to be $\delta d_L/d_L = \sqrt{(\Delta d_L/d_L)^2 + (\tilde{\Delta}d_L/d_L)^2}$.

Similarly, the relation (28) can be formally written as

$$\Delta q_0 = \frac{A_{q_0}}{\sqrt{N}}, \quad (29)$$

where N is the number of the effective GW events. The coefficient A_{q_0} is given by

$$A_{q_0}^{-2} = \int_0^{z_{\max}} \left(\frac{\partial \ln d_L(z)}{\partial q_0} \right)^2 f(z) \left\langle \frac{1}{(\delta d_L/d_L(\hat{\gamma}, z))^2} \right\rangle_{\hat{\gamma}} dz, \quad (30)$$

where $f(z)$ is the number distribution of GW sources over redshift z , that is normalized by the total number of events so that its integration over z yields unity. In this paper, we

assume that the GW sources are uniformly distributed in the comoving volume.

We evaluate numerically A_{q_0} and the fraction of selected events f_{q_0} by simulating 10^5 random samples of BNSs and NSBHs with random sky directions, inclination angles and polarization angles. The samples are uniformly distributed in the comoving volume in the range $z < 2$. The fraction of effective samples is also defined by $f_{q_0} = N_{\text{eff}}/N_{\text{tot}}$. The values of A_{q_0} and f_{q_0} quantify the measurement accuracy of q_0 by the detector network, and are listed in Tables II and III for BNSs and NSBHs, respectively. Consistent with the previous results, for the 2CE network, we find that only a small fraction of binary coalescences satisfy the selection criteria with $f_{q_0} = 3.98\%$ for BNSs and 6.29% for NSBHs. For the CE-ETD network, we find that the values of f_{q_0} are ten times larger. While for the rest of the networks studied, around 70% or more sources can satisfy the selection criteria and are used to measure q_0 . For these networks, $\Delta q_0 \sim 0.02$ can be achieved if we select 100 BNSs or NSBHs with known redshift, which is already similar to the best accuracy available at this writing. Note the uncertainty of our estimation mainly depends on the number of the selected GW events, with accurate redshift information, that is much smaller than the total number of observable GW events in this redshift range ($\sim 10^7$ per year for BNSs) [21].

⁶For biased estimation method, we also need to consider systematic errors.

TABLE II. The constraints of Hubble constant H_0 and deceleration parameter q_0 , and EoS of dark energy derived from 10^5 randomly distributed BNS samples.

	2CE	CE-ETD	2ETD	3CE	3ETD	3cETD	4ETD
A_{H_0}	0.077	0.082	0.029	0.015	0.022	0.022	0.019
f_{H_0}	81.4%	90.6%	97.8%	99.7%	98.8%	99.1%	99.5%
A_{q_0}	0.335	0.337	0.262	0.160	0.216	0.216	0.193
f_{q_0}	3.98%	38.0%	66.3%	77.2%	75.6%	77.6%	80.5%
A'_{q_0}	0.071	0.088	0.092	0.068	0.084	0.082	0.078
f'_{q_0}	100%	100%	100%	100%	100%	100%	100%
A_{w_0}	1.007	1.506	1.350	0.959	1.216	1.197	1.124
A_{w_a}	6.326	8.963	8.380	6.040	7.572	7.457	7.020
A_{FoM}	0.517	0.280	0.295	0.566	0.361	0.372	0.420

TABLE III. Same as Table II, but here the NSBHs, instead of BNSs, are considered.

	2CE	CE-ETD	2ETD	3CE	3ETD	3cETD	4ETD
A_{H_0}	0.092	0.056	0.048	0.025	0.037	0.037	0.032
f_{H_0}	97.4%	100%	100%	100%	100%	100%	100%
A_{q_0}	0.362	0.239	0.213	0.143	0.177	0.175	0.158
f_{q_0}	6.29%	61.3%	76.4%	84.9%	83.7%	85.0%	87.5%
A'_{q_0}	0.066	0.070	0.080	0.065	0.074	0.073	0.071
f'_{q_0}	100%	100%	100%	100%	100%	100%	100%
A_{w_0}	1.012	1.104	1.334	0.965	1.211	1.194	1.126
A_{w_a}	6.259	6.760	8.015	6.008	7.341	7.243	6.875
A_{FoM}	0.549	0.476	0.347	0.590	0.410	0.421	0.463

It has been argued that for high- z binary coalescence GW events, the most promising method to measure their redshifts is to observe their GRB counterparts and afterglows [98]. On the other hand, GRBs are believed to be beamed: the γ radiation is emitted in a narrow cone more or less perpendicular to the binary orbital plane, and the observed GRBs are nearly all beamed towards the Earth. For those face-on binaries with observed GRB counterparts, the sky direction (θ_s, ϕ_s), inclination angle ι , and polarization angle ψ_s can be determined precisely by the EM observation, therefore should be excluded in the Fisher matrix analysis. We repeat the same calculation for 10^5 face-on GW sources in the redshift $z < 2$ as above but adopting five-parameter Fisher matrix, and recalculate A'_{q_0} and f'_{q_0} (listed in Tables II and III), which mimic A_{q_0} and f_{q_0} , respectively. Note that, the quantity $\hat{\gamma}$ in this case represents $(\theta_s, \phi_s, \psi_s)$, instead of $(\theta_s, \phi_s, \iota, \psi_s)$.

We find that in this case, the uncertainty of distance become much smaller than that from the nine-parameter Fisher matrix analysis. All the simulated samples can satisfy the selection criteria, regardless of the network configurations. Due to larger SNRs of these face-on sources, the detector networks consisting of one or more CEs yield the best measurement accuracy of q_0 . For a conservative estimation of 1000 observed BNSs or NSBHs as in previous works [21,22], we have $\Delta q_0 \sim 0.002$, which

is 10 times smaller than the best measurement available presently. For other networks, the constraint becomes slightly less stringent, and the values of Δq_0 is $\sim 20\%$ larger for two-detector or three-detector networks, and $\sim 10\%$ larger for four-detector networks. We should emphasize that, although the detector networks consisting of at least one ET-D give a slightly worse constraint on q_0 for the same number of the observed events, these networks yield a much better angular resolution for GW sources, which could be helpful to hunt for their EM counterparts, and greatly increase the total number of events with known redshift information.

C. Determination of cosmic dark energy

A possible explanation of cosmic acceleration could be the presence of dark energy, which has positive density but negative pressure (see reviews [99,100]). The key question is how well we will be able to differentiate between various dark energy models by measuring the dark energy EoS and its time evolution. A number of traditional EM methods have been used to constrain the EoS of dark energy, including using type Ia supernovae (SNIa), the temperature and polarization anisotropies of the CMB radiation, the baryon acoustic oscillations (BAO) peak in the distribution of galaxies, and weak gravitational lensing [99,100]. As mentioned above, GW standard siren provides a new method

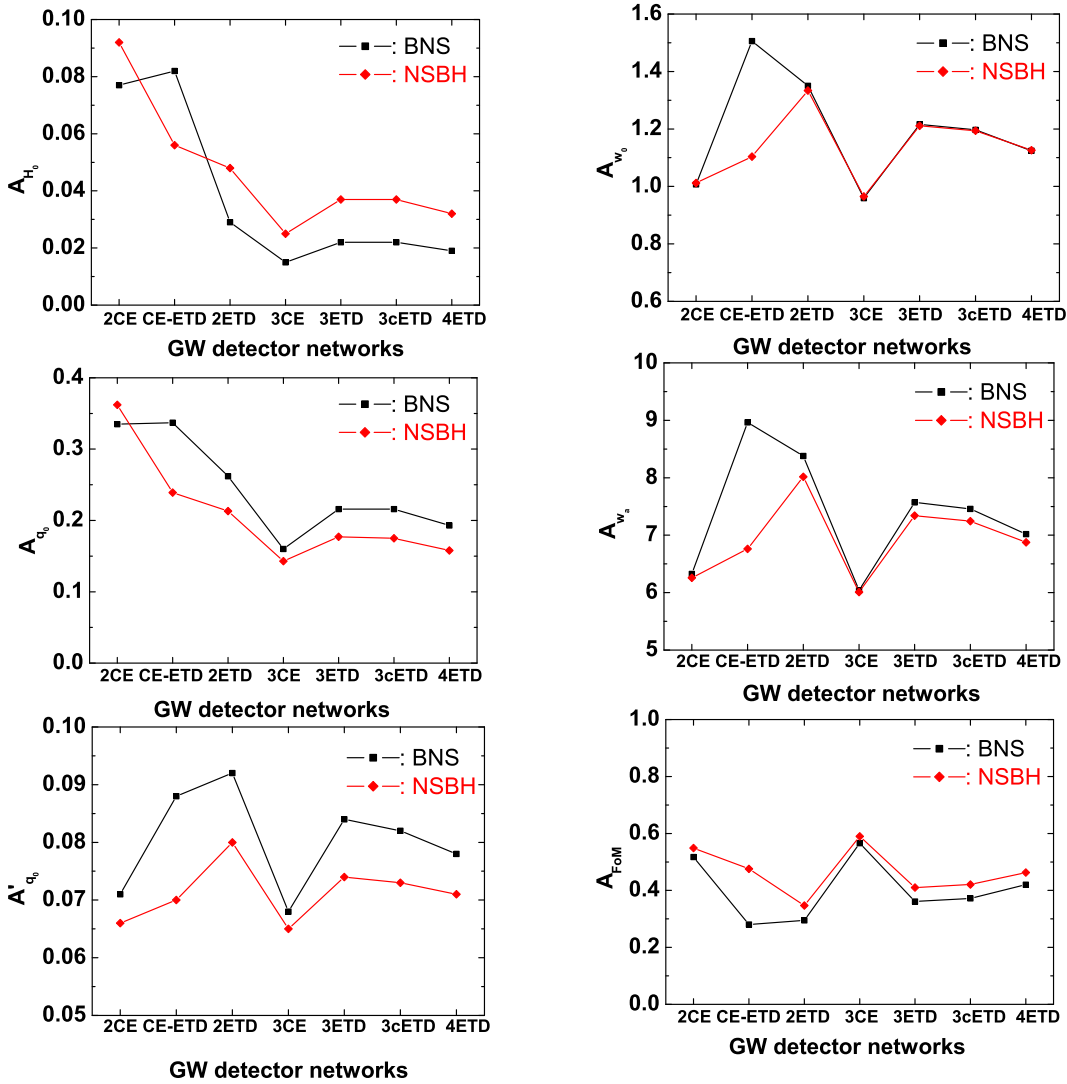


FIG. 25. The values of A_{H_0} (upper left), A_{q_0} (middle left), A'_{q_0} (lower left), A_{w_0} (upper right), A_{w_a} (middle right), $A_{F_{\text{OM}}}$ (lower right) for various GW detector networks. In each panel, the black dots denote the results derived from 10^5 randomly distributed BNS samples, and the red dots denote the results derived from 10^5 randomly distributed NSBH samples.

to probe the physics of dark energy, which have been partly discussed in the previous works [21,22] for a single ET detector. In this subsection, we extend the same analysis to the 3G detector networks.

Similar to [22], we adopt a phenomenological form for EoS parameter w as a function of redshift

$$w(z) \equiv \frac{p_{\text{de}}}{\rho_{\text{de}}} = w_0 + w_a \frac{z}{1+z}, \quad (31)$$

where p_{de} and ρ_{de} are the pressure and energy density of dark energy, respectively. This is the widely adopted Chevalier-Polarski-Linder form in the literature [100,101]. In this form, w_0 is the present EoS and w_a quantifies its evolution with redshift. In the Λ CDM model, dark energy is described by the cosmological constant, which has $w_0 = -1$ and $w_a = 0$. We consider a general FLRW universe, in which the luminosity

distance of astrophysical sources as a function of redshift z is given by [97]

$$d_L(z) = (1+z) \begin{cases} |k|^{-1/2} \sin \left[|k|^{1/2} \int_0^z \frac{dz'}{H(z')} \right] & (\Omega_k < 0), \\ \int_0^z \frac{dz'}{H(z')} & (\Omega_k = 0), \\ |k|^{-1/2} \sinh \left[|k|^{1/2} \int_0^z \frac{dz'}{H(z')} \right] & (\Omega_k > 0), \end{cases} \quad (32)$$

where $|k|^{1/2} \equiv H_0 \sqrt{|\Omega_k|}$ and Ω_k is the contribution of spatial curvature to the critical density. The Hubble parameter $H(z)$ is given by

$$H(z) = H_0 [\Omega_m (1+z)^3 + \Omega_k (1+z)^2 + (1-\Omega_m-\Omega_k) E(z)]^{1/2}, \quad (33)$$

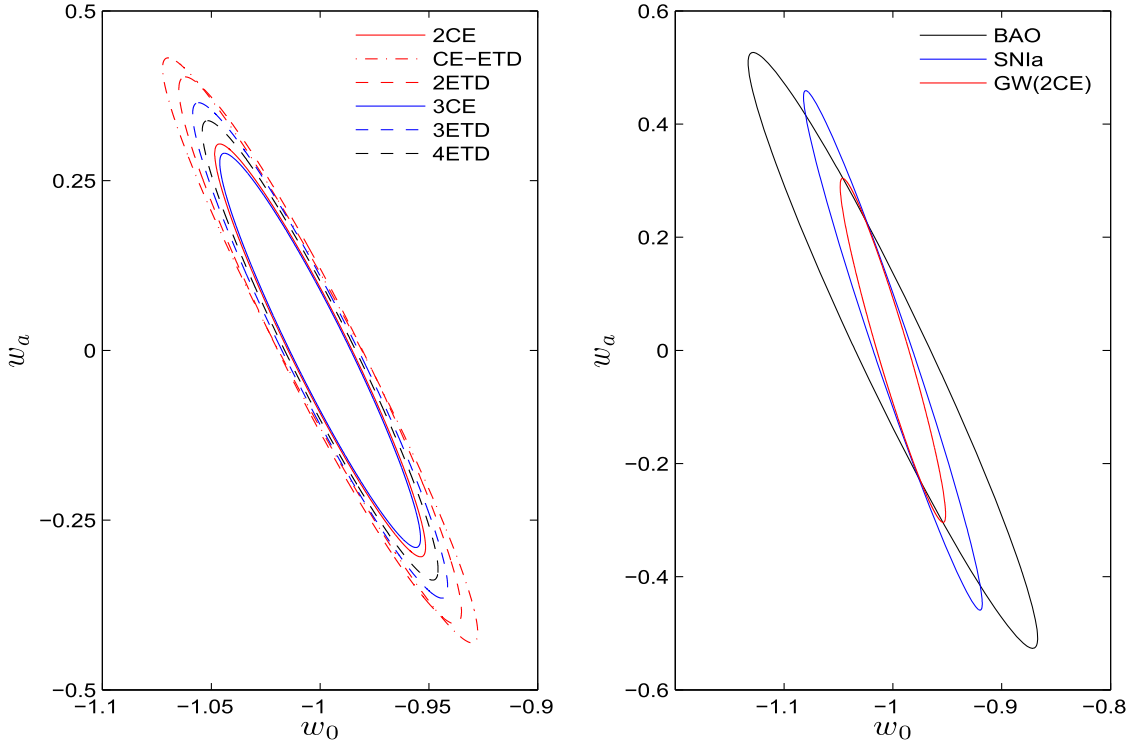


FIG. 26. The two-dimensional uncertainty contours of the dark energy parameters w_0 and w_a for various detection methods. Note that, in the case of GW detector networks, we assumed that 1000 face-on BNS sources are observed.

where the function $E(z)$ is defined as

$$E(z) = (1+z)^{3(1+w_0+w_a)} e^{-3w_a z/(1+z)}. \quad (34)$$

From the expression of d_L , it seems possible that one can constrain the full parameter set $(H_0, \Omega_m, \Omega_k, w_0, w_a)$ together by the GW data alone, as long as the redshifts of GW sources are known. Unfortunately, in the previous work [22], we found this globe constraints cannot be realized, due to the strong degeneracy between the background parameters $(H_0, \Omega_m, \Omega_k)$ and the dark energy parameters (w_0, w_a) . The same problem also happens in other methods for dark energy detection (e.g., SNIa and BAO methods). A general way to break this degeneracy is to combine the result with the CMB data, which are sensitive to the background parameters $(H_0, \Omega_m, \Omega_k)$, and provide the necessary complementarity to the GW data. It has also been discovered in [22] that, taking the CMB observation as a prior is nearly equivalent to treat the parameters $(H_0, \Omega_m, \Omega_k)$ as known in data analysis. Thus, we use the GW data to constrain the parameters (w_0, w_a) only.

In order to estimate the errors of these parameters, we study a Fisher matrix F_{ij} for a collection of inspiral events, which is given by

$$F_{ij} = \sum_k \frac{(\partial \ln d_L(k)/\partial p_i)(\partial \ln d_L(k)/\partial p_j)}{(\delta d_L/d_L(k))^2}, \quad (35)$$

where the indices i and j run from 1 to 2, for the two free parameters (w_0, w_a) . The index $k = 1, 2, \dots, N$, labels the event at $(z_k, \hat{\gamma}_k)$ among the total N sources. The value of $\delta d_L/d_L$ includes both the statistical error and the weak-lensing error. The uncertainties of dark energy parameters are given by $\Delta w_0 = (F^{-1})_{11}$ and $\Delta w_a = (F^{-1})_{22}$. To estimate and compare the goodness of constraints from the observational data sets, we calculate the figure of merit (FoM) [100], for each data sets, which is proportional to the inverse area of the error ellipse in the $w_0 - w_a$ plane,

$$\text{FoM} = [\text{Det}C(w_0, w_a)]^{-1/2}, \quad (36)$$

where $C(w_0, w_a)$ is the covariance matrix of w_0 and w_a . Larger FoM means stronger constraint on the parameters since it corresponds to a smaller error ellipse. Similar to the discussion of q_0 constraint above, we consider only the face-on sources with known redshift and calculate their distance uncertainties with the five-parameter Fisher matrix. We adopt a fiducial cosmological model with the values of parameters given by Planck Collaboration in [82].

When the number of events is large, the sum over events in Eq. (35) can be replaced by the following integral [22],

$$F_{ij} = N \times \int_0^{z_{\max}} \frac{\partial \ln d_L(z)}{\partial p_i} \frac{\partial \ln d_L(z)}{\partial p_j} \times f(z) \left\langle \frac{1}{(\delta d_L/d_L(\hat{\gamma}, z))^2} \right\rangle_{\hat{\gamma}} dz. \quad (37)$$

The numerical calculation, based on 10^5 random samples, gives the following results

$$\Delta w_0 = \frac{A_{w_0}}{\sqrt{N}}, \quad \Delta w_a = \frac{A_{w_a}}{\sqrt{N}}, \quad \text{FoM} = A_{\text{FoM}} N. \quad (38)$$

The values of the coefficients A_{w_0} , A_{w_a} and A_{FoM} for various detector networks are listed in Tables II and III.

In Fig. 26, we plot the two-dimensional uncertainty contours of various detector networks for demonstration. For a conservative estimation with 1000 selected BNSs, for the 2CE network, we obtain,

$$\Delta w_0 = 0.032, \quad \Delta w_a = 0.20, \quad \text{FoM} = 517. \quad (39)$$

We find that the constraints of w_0 and w_a are 2 times more stringent than the results for an single ET detector, derived in previous work [22]. For the 3CE network, the results are similar, with $\Delta w_0 = 0.030$, $\Delta w_a = 0.19$ and $\text{FoM} = 566$. However, for the network consisting of at least one ET-D detector, the uncertainties are slightly larger, due to smaller SNRs. For instance, for the 2ETD network, we obtain $\Delta w_0 = 0.043$, $\Delta w_a = 0.26$ and $\text{FoM} = 295$, which become $\Delta w_0 = 0.036$, $\Delta w_a = 0.22$ and $\text{FoM} = 420$ for the 4ETD network.

We compare the capability of the 3G detectors in constraining the EoS of the dark energy with that of traditional EM methods, following the same analyses as in [22] for SNIa method and BAO method. For the future SNIa survey, we considered the SNAP (Supernova/Acceleration Probe) project [100,102], which considered 300 low redshift supernovae, uniformly distributed over $z \in (0.03, 0.08)$, and 2000 high redshift supernovae in the range $z \in (0.1, 1.7)$. For the potential BAO observation, we considered the final JDEM (Joint Dark Energy Mission) project [100,103], which is expected to survey the galaxies of 10,000 deg² in the redshift range $z \in (0.5, 2)$. The corresponding two-dimensional uncertainty contours of these two projects are also plotted in Fig. 26, from which we find that with the 2CE 3G GW detector network, the constraints of dark energy parameters are significantly more stringent than the traditional SNIa and BAO methods, using conservatively only 1000 GW events.

VII. CONCLUSIONS

The detection of GW sources opens the possibility of using a brand new GW window to further our understanding of fundamental physics, cosmology and astrophysics. The coalescing compact binaries are the prime sources of ground-based detectors. The localization of them, including the angular resolution and the distance determination, is one of the key tasks for the GW observations. As the standard sirens, the luminosity distance of these binary coalescence sources can be precisely measured by GW observations without the aid of any

cosmic distance ladder. Meanwhile, the accurate localization of GW sources is helpful for the identification of their host galaxies or the follow-up observations on the EM counterparts, which enables independent measurements of their redshifts. Thus, the distance-redshift relation can be used to measure the expansion history of the Universe, including the determination of the Hubble constant, the acceleration of the Universe, and measuring the EoS of dark energy.

In this article, we give a comprehensive discussion on the localization of GW events by 3G GW detectors, which aim to significantly increase the detection band toward frequencies as low as a few Hz. Taking into account the rotation of the Earth, a single detector can be effectively treated as a detector network with long baselines. Thus, the localization of binary coalescence sources with small masses could be greatly improved, as long as the contribution of GW signal at sub-10 Hz range is significant. In this article, we employ the standard Fisher information matrix to investigate the localization capabilities of 3G detectors, including a single detector, and the network consisting of up to four detectors with different configurations. Focusing on the ET and CE detectors, we first investigate the influence of the Earth's rotation on the localization of GW sources. We find that, for an individual 3G detector (in particular for ET), the localization of coalescing BNSs and low-mass NSBHs, can be significantly improved due to the periodic self-rotation of the Earth. This effect is much more significant for the edge-on binaries, than the face-on ones. In addition, we find that a slight reduction of the detector noise at low-frequency range, in particular in the range $f \in (1, 10)$ Hz, can significantly improve the localizations of GW sources by an individual 3G detector. For ET and an ideal detector with flat low-frequency noise level, the dependence of $\Delta\Omega_s$ and $\Delta d_L/d_L$ on the low-frequency cutoff can be approximated by a broken power-law formula.

As the main task of this article, we investigate the localization capabilities of 3G experiments as a function of redshift for BNS and NSBHs. For a network of two CE detectors, nearby BNSs or NSBHs ($z \lesssim 0.1$) can be localized with reasonable accuracy of $\Delta\Omega_s \sim 10$ deg² and $\Delta d_L/d_L < 1$. However, if at least one ET-D detector is included in the two-detector networks, the localization of GW sources can be greatly improved, due to the special configuration of ET experiment. For instance, for both BNSs and NSBHs at $z = 0.1$, we have $\Delta\Omega_s \sim 1$ deg² and $\Delta d_L/d_L \sim 0.1$. If considering a promising network consisting of four ET-D detectors in the Europe, U.S., China, and Australia, the angular resolution of the BNSs and NSBHs at $z = 0.1$ could reach the accuracy of $\Delta\Omega_s \sim 0.1$ deg² and $\Delta d_L/d_L \sim 0.003$, which might be sufficient to directly identify their host galaxies [104]. In addition, for four-detector network, the accurate localization of GW sources can be extended to higher redshifts. For BNSs and NSBHs at $z = 2$, we have $\Delta\Omega_s \sim 10$ deg², which is

comparable to the field of view of some EM telescopes (such as Pan-STARRS and SkyMapper telescope). Thus, confident identifications of their EM counterparts become possible, and these sources can be extremely important for high- z multimessenger astronomy including cosmology. Our result also show that, for an individual 3G detector and the detector networks, there is a pronounced anticorrelation between the angular resolution and the distance accuracy. For GW sources at a fixed redshift, the face-on ones yield a better angular resolution, while the edge-on ones have a better distance determination.

We discuss the implication of our result to using GW sources as an independent tool to probe the cosmological model of our Universe. In particular, we investigate how detections of GW sources by 3G detectors can help constraining the Hubble constant H_0 , the deceleration parameter q_0 , and the EoS of cosmic dark energy. We conclude that the two-detector network 2ETD, three-detector, and four-detector networks could help set stringent constraints on H_0 using BNSs or NSBH at low-redshift. Even if only 10 BNSs or NSBHs with known redshift, selected with criteria of $\text{SNR} \geq 8$ and $\Delta d_L/d_L \leq 0.5$, can be observed by one of these detector networks, the accuracy of H_0 can be achieved at 0.9% or less, which is 2 times smaller than the currently best accuracy. In addition, we find that the edge-on sources, instead of the face-on sources, dominate the constraint of H_0 due to better $\Delta d_L/d_L$ for edge-on ones. For constraining q_0 , we find that the capabilities of various 3G detector

networks are similar. Considering the face-on GW events at the redshift range $z < 2$, for which the redshifts are possible to be measured from their EM counterparts, we find that if 1000 events can be selected, $\Delta q_0 \sim 0.002$ could be achieved, which is around 10 times better than the currently best values. These 1000 face-on events can also constrain the EoS of cosmic dark energy with accuracies $\Delta w_0 \sim 0.03$ and $\Delta w_a \sim 0.2$, which are more stringent than the projected accuracies for the future JDEM BAO project and the SNAP SNIa observations. These results show that the cosmography with 3G detector networks is extremely promising, which provides an independent method to probe our Universe up to the high redshift range.

ACKNOWLEDGMENTS

We appreciate the helpful discussions with Man Leong Chan, Ik Siong Heng, Martin Hendry, Yiming Hu, Christopher Messenger, David Blair, Chunrong Zhao, and Li Ju. W.Z. is supported by NSFC Grants No. 11773028, No. 11603020, No. 11633001, No. 11173021, No. 11322324, No. 11653002, and No. 11421303, the project of Knowledge Innovation Program of the Chinese Academy of Science, the Fundamental Research Funds for the Central Universities, and the Strategic Priority Research Program of the Chinese Academy of Sciences Grant No. XDB23010200. L.W.'s research is supported in part by the Australian Research Council.

-
- [1] B. P. Abbott *et al.* (LIGO Scientific and Virgo Collaborations), *Phys. Rev. Lett.* **116**, 061102 (2016); *Phys. Rev. D* **93**, 122003 (2016); *Phys. Rev. Lett.* **116**, 241102 (2016); **116**, 131103 (2016).
 - [2] B. P. Abbott *et al.* (LIGO Scientific and Virgo Collaborations), *Astrophys. J.* **826**, L13 (2016); *Astrophys. J. Suppl. Ser.* **225**, 8 (2016).
 - [3] B. P. Abbott *et al.* (LIGO Scientific and Virgo Collaborations), *Phys. Rev. D* **94**, 064035 (2016).
 - [4] B. P. Abbott *et al.* (LIGO Scientific and Virgo Collaborations), *Phys. Rev. Lett.* **116**, 241103 (2016).
 - [5] B. P. Abbott *et al.* (LIGO Scientific and Virgo Collaborations), *Phys. Rev. Lett.* **118**, 221101 (2017).
 - [6] B. P. Abbott *et al.* (LIGO Scientific and Virgo Collaborations), *Astrophys. J.* **851**, L35 (2017).
 - [7] B. P. Abbott *et al.* (LIGO Scientific and Virgo Collaborations), *Phys. Rev. Lett.* **119**, 141101 (2017).
 - [8] B. P. Abbott *et al.* (LIGO Scientific and Virgo Collaborations), *Phys. Rev. Lett.* **119**, 161101 (2017).
 - [9] B. P. Abbott *et al.* (LIGO Scientific and Virgo Collaborations), *Phys. Rev. D* **93**, 122003 (2016); *Phys. Rev. X* **6**, 041015 (2016).
 - [10] J. Aasi *et al.* (The LIGO Scientific Collaboration), *Classical Quantum Gravity* **32**, 115012 (2015).
 - [11] F. Acernese *et al.*, *Classical Quantum Gravity* **32**, 024001 (2015).
 - [12] Y. Aso, Y. Michimura, K. Somiya, M. Ando, O. Miyakawa, T. Sekiguchi, D. Tatsumi, and H. Yamamoto, *Phys. Rev. D* **88**, 043007 (2013); B. P. Abbott *et al.* (KAGRA Collaboration, LIGO Scientific Collaboration and Virgo Collaborations), *Living Rev. Relativity* **19**, 1 (2016).
 - [13] B. Iyer, T. Souradeep, C. Unnikrishnan, S. Dhurandhar, S. Raja, A. Kumar, and A. S. Sengupta, LIGO-India Tech. Rep. (2011), <https://dcc.ligo.org/cgi-bin/DocDB>ShowDocument?docid=75988>.
 - [14] M. Punturo *et al.*, *Classical Quantum Gravity* **27**, 194002 (2010).
 - [15] M. Abernathy *et al.*, Einstein Gravitational Wave Telescope: Conceptual Design Study, Document No. ET-0106A-10.
 - [16] The Einstein Telescope Project, <https://www.et-gw.eu/>.
 - [17] B. P. Abbott *et al.*, *Classical Quantum Gravity* **34**, 044001 (2017).
 - [18] S. Dwyer, D. Sigg, S. W. Ballmer, L. Barsotti, N. Mavalvala, and M. Evans, *Phys. Rev. D* **91**, 082001 (2015).

- [19] M. Punturo *et al.*, *Classical Quantum Gravity* **27**, 084007 (2010).
- [20] S. Hild *et al.*, *Classical Quantum Gravity* **28**, 094013 (2011).
- [21] B. S. Sathyaprakash, B. Schutz, and C. van den Broeck, *Classical Quantum Gravity* **27**, 215006 (2010).
- [22] W. Zhao, C. van den Broeck, D. Baskaran, and T. G. F. Li, *Phys. Rev. D* **83**, 023005 (2011).
- [23] S. R. Taylor and J. R. Gair, *Phys. Rev. D* **86**, 023502 (2012).
- [24] R. Cai and T. Yang, *Phys. Rev. D* **95**, 044024 (2017).
- [25] A. Piorkowska, M. Biesiada, and Z. Zhu, *J. Cosmol. Astropart. Phys.* **10** (2013) 022; M. Biesiada, X. Ding, A. Piorkowska, and Z. Zhu, *J. Cosmol. Astropart. Phys.* **10** (2014) 080; X. Ding, M. Biesiada, and Z. Zhu, *J. Cosmol. Astropart. Phys.* **12** (2015) 006.
- [26] T. Regimbau *et al.*, *Phys. Rev. D* **86**, 122001 (2012); T. Regimbau, D. Meacher, and M. Coughlin, *Phys. Rev. D* **89**, 084046 (2014); D. Meacher, K. Cannon, C. Hanna, T. Regimbau, and B. S. Sathyaprakash, *Phys. Rev. D* **93**, 024018 (2016).
- [27] J. R. Gair, I. Mandel, M. C. Miller, and M. Volonteri, *Gen. Relativ. Gravit.* **43**, 485 (2011); E. A. Huerta and J. R. Gair, *Phys. Rev. D* **83**, 044021 (2011).
- [28] B. Sathyaprakash *et al.*, arXiv:1108.1423; *Classical Quantum Gravity* **29**, 124013 (2012); C. van den Broeck, *J. Phys. Conf. Ser.* **484**, 012008 (2014).
- [29] C. K. Mishra, K. G. Arun, B. R. Iyer, and B. S. Sathyaprakash, *Phys. Rev. D* **82**, 064010 (2010).
- [30] W. D. Pozzo, T. G. F. Li, and C. Messenger, *Phys. Rev. D* **95**, 043502 (2017).
- [31] C. Messenger and J. Read, *Phys. Rev. Lett.* **108**, 091101 (2012).
- [32] S. Vitale and M. Evans, *Phys. Rev. D* **95**, 064052 (2017).
- [33] X. Zhang, J. M. Yu, T. Liu, W. Zhao, and A. Z. Wang, *Phys. Rev. D* **95**, 124008 (2017); X. Zhang, T. Liu, and W. Zhao, *Phys. Rev. D* **95**, 104027 (2017).
- [34] K. G. Arun and A. Pai, *Int. J. Mod. Phys. D* **22**, 1341012 (2013).
- [35] X. Fan, K. Liao, M. Biesiada, A. Piorkowska-Kurpas, and Z. Zhu, *Phys. Rev. Lett.* **118**, 091102 (2017); K. Liao, X. Fan, X. Ding, M. Biesiada, and Z. Zhu, *Nat. Commun.* **8**, 1148 (2017).
- [36] B. S. Sathyaprakash and B. F. Schutz, *Living Rev. Relativity* **12**, 2 (2009).
- [37] B. F. Schutz, *Nature (London)* **323**, 310 (1986).
- [38] S. Nissanke, S. A. Hughes, D. E. Holz, N. Dalal, and J. L. Sievers, *Astrophys. J.* **725**, 496 (2010); S. Nissanke, D. E. Holz, N. Dalal, and S. A. Hughes, arXiv:1307.2638.
- [39] C. L. MacLeod and C. J. Hogan, *Phys. Rev. D* **77**, 043512 (2008).
- [40] D. E. Holz and S. A. Hughes, *Astrophys. J.* **629**, 15 (2005).
- [41] N. Dalal, D. E. Holz, S. A. Hughes, and B. Jain, *Phys. Rev. D* **74**, 063006 (2006).
- [42] K. G. Arun, B. R. Iyer, B. S. Sathyaprakash, S. Sinha, and C. van den Broeck, *Phys. Rev. D* **76**, 104016 (2007); K. G. Arun, C. K. Mishra, C. van den Broeck, B. R. Iyer, B. S. Sathyaprakash, and S. Sinha, *Classical Quantum Gravity* **26**, 094021 (2009); C. van den Broeck, M. Trias, B. S. Sathyaprakash, and A. M. Sintes, *Phys. Rev. D* **81**, 124031 (2010); A. Stavridis, K. G. Arun, and C. M. Will, *Phys. Rev. D* **80**, 067501 (2009); S. Babak, J. R. Gair, A. Petiteau, and A. Sesana, *Classical Quantum Gravity* **28**, 114001 (2011); N. Tamanini, C. Caprini, E. Barausse, A. Sesana, A. Klein, and A. Petiteau, *J. Cosmol. Astropart. Phys.* **04** (2016) 002; R. G. Cai, N. Tamanini, and T. Yang, *J. Cosmol. Astropart. Phys.* **05** (2017) 031.
- [43] C. Cutler and D. E. Holz, *Phys. Rev. D* **80**, 104009 (2009); S. Camera and A. Nishizawa, *Phys. Rev. Lett.* **110**, 151103 (2013).
- [44] C. M. Will, *Theory and Experiment in Gravitational Physics* (Cambridge University Press, Cambridge, England, 1993); *Living Rev. Relativity* **17**, 4 (2014).
- [45] C. M. Will, *Phys. Rev. D* **50**, 6058 (1994); J. Alsing, E. Berti, C. M. Will, and H. Zaglauer, *Phys. Rev. D* **85**, 064041 (2012); P. D. Scharre and C. M. Will, *Phys. Rev. D* **65**, 042002 (2002); C. M. Will and N. Yunes, *Classical Quantum Gravity* **21**, 4367 (2004).
- [46] L. Blanchet and B. S. Sathyaprakash, *Phys. Rev. Lett.* **74**, 1067 (1995).
- [47] F. D. Ryan, *Phys. Rev. D* **56**, 1845 (1997).
- [48] K. G. Arun, B. R. Iyer, M. S. S. Qusailah, and B. S. Sathyaprakash, *Classical Quantum Gravity* **23**, L37 (2006).
- [49] B. P. Abbott *et al.* (LIGO Scientific and Virgo Collaborations), *Phys. Rev. Lett.* **116**, 221101 (2016).
- [50] L. E. Fesik, Yu. V. Baryshev, V. V. Sokolov, and G. Paturel, arXiv:1702.03440.
- [51] N. Yunes and F. Pretorius, *Phys. Rev. D* **80**, 122003 (2009); N. Loutrel, N. Yunes, and F. Pretorius, *Phys. Rev. D* **90**, 104010 (2014); N. Yunes, K. Yagi, and F. Pretorius, *Phys. Rev. D* **94**, 084002 (2016).
- [52] Z. Cao, P. Galaviz, and L. Li, *Phys. Rev. D* **87**, 104029 (2013).
- [53] E. Berti, E. Barausse, V. Cardoso *et al.*, *Classical Quantum Gravity* **32**, 243001 (2015).
- [54] B. P. Abbott *et al.* (LIGO Scientific and Virgo Collaborations), *Phys. Rev. Lett.* **120**, 031104 (2018).
- [55] B. P. Abbott *et al.* (LIGO Scientific and Virgo Collaborations), *Phys. Rev. D* **93**, 122008 (2016); **95**, 042003 (2017); *Astrophys. J.* **841**, 89 (2017); M. G. Aartsen *et al.* (ANTARES Collaboration, IceCube Collaboration, LIGO Scientific Collaboration, and Virgo Collaboration), *Phys. Rev. D* **90**, 102002 (2014); **93**, 122010 (2016); **96**, 022005 (2017); Q. Chu, E. J. Howell, A. Rowlinson, H. Gao, B. Zhang, S. J. Tingay, M. Boer, and L. Wen, *Mon. Not. R. Astron. Soc.* **459**, 121 (2016).
- [56] K. Thorne, in *300 Years of Gravitation*, edited by S. W. Hawking and W. Israel (Cambridge University Press, Cambridge, England, 1987).
- [57] B. Schutz, *Classical Quantum Gravity* **28**, 125023 (2011).
- [58] Y. Gursel and M. Tinto, *Phys. Rev. D* **40**, 3884 (1989).
- [59] P. Jaradowski and A. Krolak, *Phys. Rev. D* **49**, 1723 (1994).
- [60] A. Pai, S. Dhurandhar, and S. Bose, *Phys. Rev. D* **64**, 042004 (2001).
- [61] J. Sylvestre, *Astrophys. J.* **591**, 1152 (2003).
- [62] F. Cavalier, M. Barsuglia, M.-A. Bizouard, V. Brisson, A.-C. Clapson, M. Davier, P. Hello, S. Kreckelbergh, N. Leroy, and M. Varvelly, *Phys. Rev. D* **74**, 082004 (2006).

- [63] S. Klimenko, G. Vedovato, M. Drago, G. Mazzolo, G. Mitselmakher, C. Pankow, G. Prodi, V. Re, F. Salemi, and I. Yakushin, *Phys. Rev. D* **83**, 102001 (2011).
- [64] P. Jaranowski and A. Krolak, *Living Rev. Relativity* **8**, 3 (2005), and references therein.
- [65] L. Wen and Y. Chen, *Phys. Rev. D* **81**, 082001 (2010).
- [66] S. Fairhurst, *New J. Phys.* **11**, 123006 (2009); *Classical Quantum Gravity* **28**, 105021 (2011).
- [67] J. Veitch and A. Veccio, *Phys. Rev. D* **81**, 062003 (2010); J. Veitch *et al.*, *Phys. Rev. D* **91**, 042003 (2015); N. J. Cornish and T. B. Littenberg, *Classical Quantum Gravity* **32**, 135012 (2015); L. P. Singer and L. R. Price, *Phys. Rev. D* **93**, 024013 (2016).
- [68] B. P. Abbott *et al.*, *Living Rev. Relativity* **19**, 1 (2016).
- [69] S. Ma, Z. Cao, C. Y. Lin, H. P. Pan, and H. J. Yo, *Phys. Rev. D* **96**, 084046 (2017).
- [70] L. Wen and B. F. Schutz, *Classical Quantum Gravity* **22**, S1321 (2005).
- [71] K. Chatzioannou, N. Yunes, and N. Cornish, *Phys. Rev. D* **86**, 022004 (2012).
- [72] C. M. Will, *Theory and Experiment in Gravitational Physics* (Cambridge University Press, Cambridge, Engand, 1993).
- [73] J. Mills, V. Tiwari, and S. Fairhurst, arXiv:1708.00806.
- [74] R. Essick, S. Vitale, and M. Evans, *Phys. Rev. D* **96**, 084004 (2017).
- [75] P. Jaranowski, A. Krolak, and B. F. Schutz, *Phys. Rev. D* **58**, 063001 (1998).
- [76] M. Maggiore, *Gravitational Waves. Vol. 1: Theory and Experiments* (Oxford University Press, New York, 2007).
- [77] C. Cutler *et al.*, *Phys. Rev. Lett.* **70**, 2984 (1993).
- [78] L. Blanchet, *Living Rev. Relativity* **5**, 3 (2002); T. Damour, P. Jaranowski, and G. Schäfer, *Phys. Lett. B* **513**, 147 (2001); Y. Itoh, T. Futamase, and H. Asada, *Phys. Rev. D* **63**, 064038 (2001); L. Blanchet, G. Faye, B. R. Iyer, and B. Joguet, *Phys. Rev. D* **65**, 061501(R) (2002); **71**, 129902(E) (2005); Y. Itoh and T. Futamase, *Phys. Rev. D* **68**, 121501(R) (2003); Y. Itoh, *Phys. Rev. D* **69**, 064018 (2004); L. Blanchet, T. Damour, and G. Esposito-Farèse, *Phys. Rev. D* **69**, 124007 (2004); L. Blanchet, T. Damour, G. Esposito-Farèse, and B. R. Iyer, *Phys. Rev. Lett.* **93**, 091101 (2004); Y. Itoh, *Classical Quantum Gravity* **21**, S529 (2004); L. Blanchet and B. R. Iyer, *Phys. Rev. D* **71**, 024004 (2005).
- [79] L. S. Finn, *Phys. Rev. D* **46**, 5236 (1992); L. S. Finn and D. F. Chernoff, *Phys. Rev. D* **47**, 2198 (1993).
- [80] V. J. Martinez, E. Saar, E. Martinez-Gonzales, and M.-J. Pons-Borderia, *Data Analysis in Cosmology* (Springer, Berlin, 2010).
- [81] H. Cramer, *Mathematical Methods of Statistics* (Princeton University Press, Princeton, N.J., 1946).
- [82] Planck Collaboration, *Astron. Astrophys.* **594**, A13 (2016).
- [83] A. Freise, S. Chelkowski, S. Hild, W. Del Pozzo, A. Perreca, and A. Veccio, *Classical Quantum Gravity* **26**, 085012 (2009).
- [84] S. Hild *et al.*, *Classical Quantum Gravity* **28**, 094013 (2011).
- [85] C. Cutler, *Phys. Rev. D* **57**, 7089 (1998).
- [86] L. Barack and C. Cutler, *Phys. Rev. D* **69**, 082005 (2004).
- [87] P. Raffai, L. Gondan, I. S. Heng, N. Kelecsenyi, J. Logue, Z. Marka, and S. Marka, *Classical Quantum Gravity* **30**, 155004 (2013).
- [88] D. Blair *et al.*, *Sci. China-Phys. Mech. Astron.* **58**, 120402 (2015); *Sci. China-Phys. Mech. Astron.* **58**, 120405 (2015).
- [89] E. J. Howell, M. L. Chan, Q. Chu *et al.*, *Mon. Not. R. Astron. Soc.* **474**, 4385 (2018).
- [90] G. B. Zhao *et al.*, *Nature Astronomy*, **1**, 627 (2017).
- [91] C. Messenger and J. Read, *Phys. Rev. Lett.* **108**, 091101 (2012); W. Del Pozzo, T. G. F. Li, and C. Messenger, *Phys. Rev. D* **95**, 043502 (2017).
- [92] S. R. Taylor, J. R. Gair, and I. Mandel, *Phys. Rev. D* **85**, 023535 (2012); S. R. Taylor and J. R. Gair, *Phys. Rev. D* **86**, 023502 (2012).
- [93] C. Messenger, K. Takami, S. Gossan, L. Rezzolla, and B. S. Sathyaprakash, *Phys. Rev. X* **4**, 041004 (2014).
- [94] N. Seto, S. Kawamura, and T. Nakamura, *Phys. Rev. Lett.* **87**, 221103 (2001); A. Nishizawa, K. Yagi, A. Taruya, and T. Tanaka, *Phys. Rev. D* **85**, 044047 (2012); *J. Phys. Conf. Ser.* **363**, 012052 (2012).
- [95] B. P. Abbott *et al.* (LIGO Scientific and Virgo Collaboration), *Nature (London)* **551**, 85 (2017).
- [96] B. Kocsis, Z. Frei, Z. Haiman, and K. Menou, *Astrophys. J.* **637**, 27 (2006).
- [97] S. Weinberg, *Cosmology* (Oxford University Press, New York, 2008).
- [98] E. Nakar, *Phys. Rep.* **442**, 166 (2007).
- [99] L. Amendola and S. Tsujikawa, *Dark Energy* (Cambridge University Press, Cambridge, England, 2010); E. J. Copeland, M. Sami, and S. Tsujikawa, *Int. J. Mod. Phys. D* **15**, 1753 (2006); M. Li, X. D. Li, S. Wang, and Y. Wang, *Commun. Theor. Phys.* **56**, 525 (2011).
- [100] A. Albrecht, G. Bernstein, R. Cahn *et al.*, arXiv:astro-ph/0609591.
- [101] M. Chevallier and D. Polarski, *Int. J. Mod. Phys. D* **10**, 213 (2001); E. V. Linder, *Phys. Rev. Lett.* **90**, 091301 (2003).
- [102] SNAP Collaboration, arXiv:astro-ph/0405232.
- [103] A. Albrecht *et al.*, arXiv:astro-ph/0609591.
- [104] J. Loveday *et al.*, *Mon. Not. R. Astron. Soc.* **420**, 1239 (2012).